Article:
Wang, D, De Boer, G orcid.org/0000-0002-5647-1771, Neville, A et al. (1 more author) (2021) A new numerical model for investigating the effect of surface roughness on the stick and slip of contacting surfaces with identical materials. Tribology International, 159. 106947. ISSN 0301-679X

https://doi.org/10.1016/j.triboint.2021.106947

A New Numerical Model for Investigating the Effect of Surface Roughness on the Stick and Slip of Contacting Surfaces with Identical Materials

Dongze Wang[1*], Gregory De Boer[1], Anne Neville[1], Ali Ghanbarzadeh[1]

[1] School of Mechanical Engineering, University of Leeds, Leeds, UK, LS29JT

[*] Corresponding author (Dongze Wang; mn17d2w@leeds.ac.uk)

Abstract

A numerical model replicating the stick-slip contact of two elastically similar materials is presented in this paper. Based on the Coulomb's law described in the partial-slip theory of Ciavarella, the model adopts a complementary condition that facilitates the design of a novel algorithm to separate the stick and slip regions. Via the comparison between simulation results and analytical solutions, the developed model is validated and applied to study the role played by the roughness of realistic surfaces in the separation of stick and slip regions. It is found that a higher root mean square (RMS) gradient leads to smaller contacting area under constant load while the root mean square (RMS) roughness has insignificant influence if the RMS gradient is kept constant, which is in line with current literature. Under the effects of the RMS gradient, the relationship between varying skewness or kurtosis and contacting regions is irregular. Furthermore, stick regions are found to respond identically to those varying roughness factors. However, the ratio of stick regions to the total contacting region is revealed to be unaffected by the surface roughness parameters when a tangential load is applied on the contacting surfaces following a linear behaviour.

Keywords: *Partial slip, Surface roughness, Contact mechanics, Boundary element method*

1. Introduction

The problem of the combined normal and tangential loading has always been an area of interest for determining the frictional behaviour of materials in contact. In this condition, stick and slip zones may coexist presenting a 'partial slip' contact interface. The partial slip phenomenon can be commonly found in engineering practices such as fretting. The relative movement of oscillations under alternating dynamic loads is small in amplitude compared to the size of the contact area under these conditions which eventually leads to surface failure [1, 2]. In addition to fretting wear, stick-slip analysis plays an essential role when it comes to the study of rubber friction [3, 4], powder tribology [5-7] and polymer tribology [8]. Pioneering contact analysis on the stick-slip behaviour was conducted by Cattaneo [9] and Mindlin [10], who independently proposed the partial slip solution for a generally elliptical or circular contact

problem. Based on the Cattaneo-Mindlin solution, Johnson [11] developed the closed-form solution for the sliding (partial or gross) contact between two identical materials under tangential loading.

Given that the analytical solutions based on proposed assumptions are always subjected to various limitations including the simplified contact geometries and ideal loading history (usually constant), a numerical model presents itself as a suitable alternative in this dilemma. Based on finite element method (FEM) together with the domain decomposition method and boundary element method (BEM), Kosior et al. [12, 13] developed the numerical model studying the frictional elastic contact following Coulomb's law to investigate the effects of friction on the contact parameters including contact radius and normal pressure. The contact between an elastic-plastic sphere and a rigid plane in the gross slip or full stick state under the combined normal and tangential loading was simulated by Brizmer et al. [14, 15] using FEM. Notably, a large simulation domain is always required in the finite element analysis to approximate the half-space along with proper addressing of boundary conditions. This causes an enormous computational burden when analysing the contact of real rough surfaces where fine spatial discretisation is needed.

On the other hand, BEM is a more efficient method as only the boundary of the bodies needs to be discretised to characterize the surfaces. Using BEM and the conjugate gradient method (CGM), Polonsky and Keer [16] proposed a single-loop iterative CGM algorithm to solve the contact problems of rough surfaces, which served as a good reference tool for many numerical models developed in the last decade [17]. Pohrt and Li [18] proposed a displacement-controlled algorithm using CGM and BEM to solve the tangential contact problem. They converted the contact problem to an algebraic matrix equation relating the surface traction and displacement. This method identified the nodes within the non-contact region as well as stick and slip regions. Deformation for the stick nodes was always the prescribed tangential rigid body translation and shear stress for the slip nodes was always the critical value determined from the Coulomb's friction law. However, the normal and tangential contact problems are decoupled in their model, which makes it only valid for incompressible materials where Poisson's ratio is 0.5. A fully coupled model was developed by Chen and Wang using the semi-analytical method (SAM) [19], in which the algorithm is in a similar form to that of the frictionless normal contact model developed by Polonsky and Keer [16]. In their algorithm, the estimation of the tangential rigid body translation relies on analytical equations. However, the static force equilibrium was not enforced in their case and instead, they adjusted the rigid body translation according to the difference between the computed tangential force and the prescribed one. Their model was later extended to investigate the partial slip of an elastic layered half-space [20].

Inspired by the fretting model developed by Spinu and Amarandei [21, 22], a stick-slip contact model, with the same form of algorithm for both the independent normal and tangential

components, is advanced in this paper by considering the similarity between the normal contact and tangential contact problems for two elastically identical materials. With the implementation of discrete convolution, fast Fourier transform (DC-FFT), the normal contact model is developed on the basis of the CGM algorithm for contacting elastic rough surfaces by Keer and Polonsky [16]. Although the literature is continuously evolving in modelling of the stick and slip of rough surface, the criterion to separate the stick and slip regions is still ambiguous. In this paper, the Coulomb's law described in the stick-slip contact theory proposed by Ciavarella [23-25], which requires the shear traction in the stick region to always be less than the Coulomb friction, is followed to generate the complementary condition that separates the stick and slip regions for the individual tangential contact model. It should be noted that the same condition was also implemented in the partial slip contact modelling by Kosior [12, 13], Gallego [1, 26], Botto [27], Dong [28] and Bazrafshan [29]. Since a computational node exhibiting the shear stress equal to the local Coulomb friction can only happen in slip region according to the above-mentioned theory, a novel adjustment method is introduced in our algorithm of the tangential contact problem to ensure that the shear stress in the stick region is less than the critical value. Furthermore, the capability of the model to study the influence of important features of surface roughness including root mean square roughness (RMS roughness), root mean square gradient (RMS gradient), skewness and kurtosis on the stick and slip area ratios has been investigated in this paper.

2. Theory and Algorithm Description

Based on the explicit mathematical relation between the strain and stress for the contacting bodies, the BEM is implemented to develop the fully deterministic stick-slip contact model.

2.1 Problem Formulation

To start with numerical formulation, the quadratic programming approach [30] is applied to find the contact pressure and surface deformation via minimising the total complementary energy using the variational principle. For a normal contact problem of two elastic surfaces, the total complementary energy V^* is expressed as:

$$V^* = U_E^* - \int_\Omega p(u_{z0}^* + u_{z1}^*)d\Omega = U_E^* - \int_\Omega p\,\overline{u_z^*}d\Omega, \qquad \textbf{Equation 1}$$

where U_E^* is the internal complementary energy of the stressed elastic solids, Ω is the assumed contacting area where the contact pressure acts, p is the contact pressure, u_{z0}^* and u_{z1}^* are the prescribed displacement of the two contacting solids respectively and $\overline{u_z^*}$ is the total prescribed displacement of the two contacting solids inside the assumed contact domain. Therefore, the term '$\int_\Omega p\,\overline{u_z^*}d\Omega$' is the work done by the normal force.

For ideal linear elastic materials, the internal complementary energy U_E^* is numerically equal to the elastic strain energy due to the linear relation between the stress and strain as indicated in Figure 1, which is expressed as:

$$U_E^* = U_E = \frac{1}{2}\int_\Omega p\,(u_{z0} + u_{z1})\,d\Omega = \frac{1}{2}\int_\Omega p\,\overline{u_z}d\Omega \qquad \textbf{Equation 2}$$

where $\overline{u_z}$ is the composite surface displacement inside the contact zone and equals total contact deformation of two contacting solids (denoted as u_{z0} and u_{z1} correspondingly).

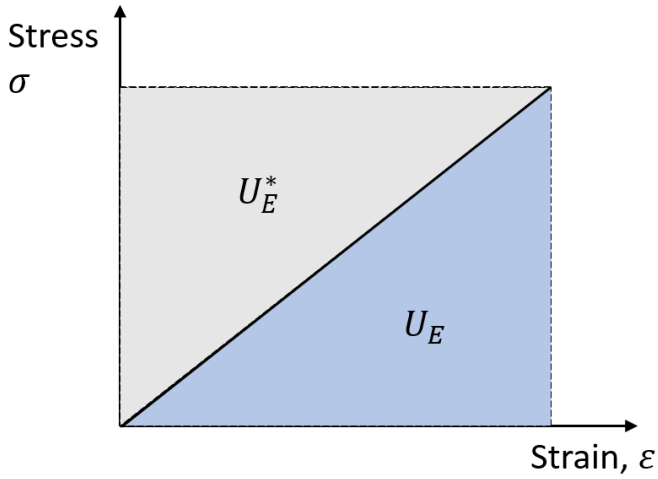

Figure 1 Relation between U_E^* and U_E for contact between linear elastic materials without plastic deformation

To express U_E^* with Equation 2 in Equation 1, the complementary potential energy for the normal contact problem is then given by:

$$V^* = \frac{1}{2}\int_\Omega p\,\overline{u_z}\,d\Omega - \int_\Omega p\overline{u_z^*}d\Omega, \qquad \textbf{Equation 3}$$

Similarly, the total complementary energy can be minimized for coupled normal and tangential contact problems in the case of linear elastic materials and is expressed as follows:

$$V^* = \frac{1}{2}\int\int t\bar{u}dxdy - \int\int t\overline{u^*}dxdy\,, \qquad \textbf{Equation 4}$$

where t is the complete surface stress vector, $\overline{u^*}$ is the prescribed displacement and $\bar{u}$ is the complete surface deformation vector determined by the following equations:

$$t = q_x e_x + q_y e_y + p e_z, \qquad \textbf{Equation 5}$$

$$\bar{u} = u_x e_x + u_y e_y + u_z e_z, \qquad \textbf{Equation 6}$$

where q_x, q_y and p are the traction force, u_x, u_y and u_z are the surface deformation and e_x, e_y and e_z are the Cartesian unit basis vectors in x, y and z directions respectively.

After discretisation, the fully coupled relationship between the contact deformation and loading can be expressed in the following matrix form:

$$\begin{bmatrix} u_x \\ u_y \\ u_z \end{bmatrix} = \begin{bmatrix} C_{xx} & C_{xy} & C_{xz} \\ C_{yx} & C_{yy} & C_{yz} \\ C_{zx} & C_{zy} & C_{zz} \end{bmatrix} \begin{bmatrix} q_x \\ q_y \\ p \end{bmatrix}, \quad \textbf{Equation 7}$$

where C_{ij} is the influence matrix of the deflection in i direction due to the load applied in j direction ($i = x, y, z$; $j = x, y, z$). The closed-form solutions of these influence coefficient matrices are provided by Ghanbarzadeh [31] and shown in Appendix A.

To simplify the stick-slip contact model, the following assumptions are made:

- Only the contact between two elastic surfaces with identical material properties is accounted for within the model. Thus, the composite shear modulus becomes zero and the Equation 7 relating the surface deformation to the traction force reduces to:

$$\begin{bmatrix} u_x \\ u_y \\ u_z \end{bmatrix} = \begin{bmatrix} C_{xx} & C_{xy} & 0 \\ C_{yx} & C_{yy} & 0 \\ 0 & 0 & C_{zz} \end{bmatrix} \begin{bmatrix} q_x \\ q_y \\ p \end{bmatrix}, \quad \textbf{Equation 8}$$

The solution of the normal contact problem is then decoupled from that of the tangential contact problem. However, the normal contact pressure is still required in advance to execute the algorithm of the tangential contact model as the Coulomb's law is followed within it to determine the critical shear traction (local Coulomb friction).

- Only the tangential force in the x-direction is considered within the model. The effect this has on the deformation in the y-direction is neglected considering the relatively large difference in the order of magnitude between the two relevant influence coefficient matrices (C_{xx} and C_{yx}) shown in Appendix B. Neglecting of the effects of stress in one specific direction on the deflections in two other directions is a common practice for many researchers when it comes to the preliminary modelling of tangential contact problems [18, 19]. Therefore, Equation 8 is further simplified to

$$\begin{bmatrix} u_x \\ 0 \\ u_z \end{bmatrix} = \begin{bmatrix} C_{xx} & 0 & 0 \\ 0 & 0 & 0 \\ 0 & 0 & C_{zz} \end{bmatrix} \begin{bmatrix} q_x \\ 0 \\ p \end{bmatrix}, \quad \textbf{Equation 9}$$

To minimise the complementary potential energy, the contact problem is to find the contact stresses and contact deformations correlated by Equation 9 which meet a series of restriction conditions. It is noteworthy that after transforming continuous functions into piecewise constant functions that are uniform within the elementary cell of the equally spaced rectangular established in the contact interface, control points for the set grid are necessary. These points are the centroids of the elements in the developed model as shown in Figure 2. Therefore, the shear traction and deformation of each element becomes the focus of the model.

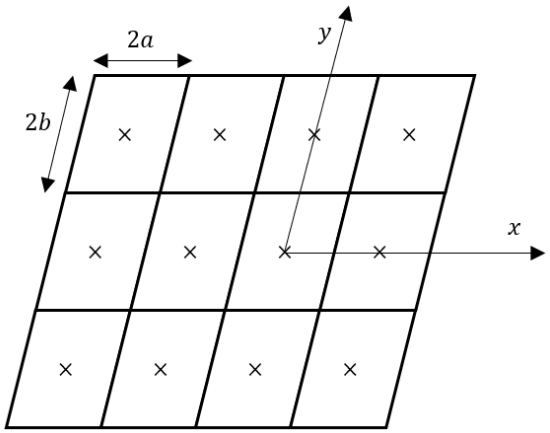

Figure 2 Discretised elements: '×' is the centroid of each element, and $2a$ and $2b$ are the side lengths of each element in x and y directions respectively

For a discretised normal contact problem, the following contact equations and inequalities should be satisfied to find those pressure and deformation:

1. Static force equilibrium: The sum of the pressure distribution at the contact interface should be equal to the applied force (W):

$$W = \Delta \sum_{(i,j)\in I_c} p(i,j), \qquad \textbf{Equation 10}$$

where Δ is the area of the element in the established mesh and equals $4ab$ indicated in Figure 2, I_c is the contact domain and i and j denote the indices of the mesh element (i,j) with $1 \leq i \leq N_1$ and $1 \leq j \leq N_2$ (N_1 and N_2 are total numbers of elements along x and y directions respectively).

2. Geometrical condition of deformation: The deformation of the surface in the normal direction should meet this geometrical condition:

$$h(i,j) = h_i(i,j) + u(i,j) - \delta, (i,j) \in I_p; \qquad \textbf{Equation 11}$$

where I_p denotes the simulation domain and h_i, h, and δ are the gap between undeformed surfaces, the gap between deformed surfaces and the normal rigid body displacement respectively as shown in Figure 3.

3. Complementary conditions should be satisfied over the contacting surfaces:

$$\begin{gathered} p(i,j) > 0 \;\&\; h(i,j) = 0, (i,j) \in I_c; \\ p(i,j) = 0 \;\&\; h(i,j) > 0, (i,j) \in I_p - I_c. \end{gathered} \qquad \textbf{Equation 12}$$

where $I_p - I_c$ denotes the non-contact domain.

As illustrated in Figure 3, the gap h for Point 1 in the range of contact radius (a_0) is 0 under the effect of the normal load. As Point 2 outside the contact radius is implying a vanishing contact pressure, there is a positive surface gap labelled as h^2. Thus, the product of the contact

pressure and surface gap is always zero over the contacting surfaces no matter which position of the interface is being referred to.

The complementary conditions shown in Equation 12 imply that the adhesion effect ($p < 0$) is not considered in this normal contact problem and the contacting surfaces are impenetrable. Inclusion of adhesion in such scenario will be complex since the introduction of non-conservative forces makes it difficult to obtain closed-form solutions based on energy approaches. However, the inclusion of the surface adhesion may become feasible by directly using the Lennard-Jones potential at the separated computational nodes. Based on a non-adhesive normal contact algorithm, a deterministic and well-validated normal contact model with adhesion was recently developed by Ghanbarzadeh [32] via the implementation of Lennard-Jones potential fields with the incorporation of a new surface integration method. This problem needs very careful consideration of energy terms as reported by Ciavarella [33, 34]. It is out of the scope of the current paper and will be the subject of future work.

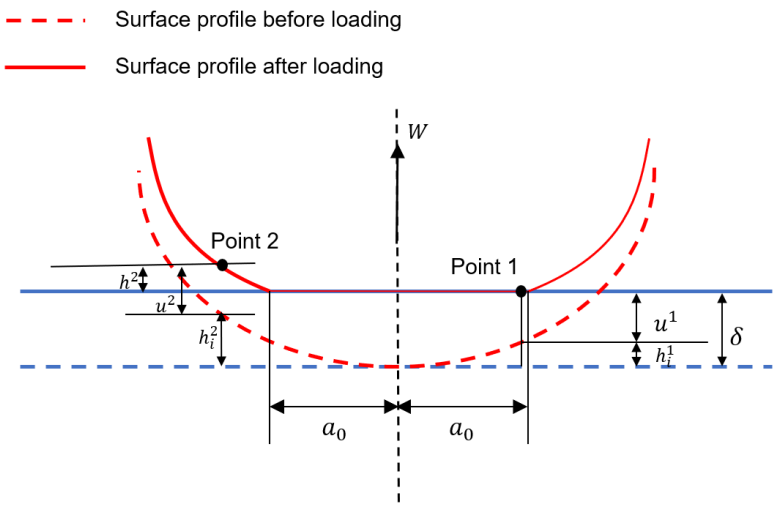

Figure 3 Displacement condition of deformation in the normal direction: h and h_i are the gap between the deformed surface and the initial surface gap respectively, u is the elastic deformation, δ is the rigid body indentation, a_0 is the contact radius, W is the applied normal load, and the superscripts 1 and 2 denote the points 1 and 2 being referred respectively.

Regarding the constraint conditions for the tangential contact problem, the following equations and inequalities must be satisfied:

1. Static force equilibrium equation:

$$\Delta \sum_{(i,j)\in I_c} q(i,j) = F_x, \qquad \textbf{Equation 13}$$

where F_x is the applied tangential force.

2. Geometrical condition of deformation:

$$s(i,j) = u_x(i,j) - \delta_x, \quad (i,j) \in I_c \qquad \textbf{Equation 14}$$

where s is the slip distance and δ_x is the right body displacement in the horizontal direction.

3. Complementary conditions should be satisfied over the contacting surfaces:

$$\begin{aligned} &|q(i,j)| < \mu p(i,j),\ s(i,j) = 0,\ \ (i,j) \in I_s; \\ &|q(i,j)| = \mu p(i,j),\ |s(i,j)| > 0,\ q(i,j) \cdot s(i,j) < 0,\ \ (i,j) \in I_c - I_s; \end{aligned} \qquad \textbf{Equation 15}$$

where μ is the coefficient of friction, I_s denotes the stick domain and $I_c - I_s$ denotes the slip domain.

As shown in Figure 4, there is no slip for the interaction region in stick state such as the Point O. When it comes to the slip region (Point A_1 and A_2), the direction of the slip (s_{x1} and s_{x2}) is always opposite to that of the applied load (F_{x1} and F_{x2}) as labelled.

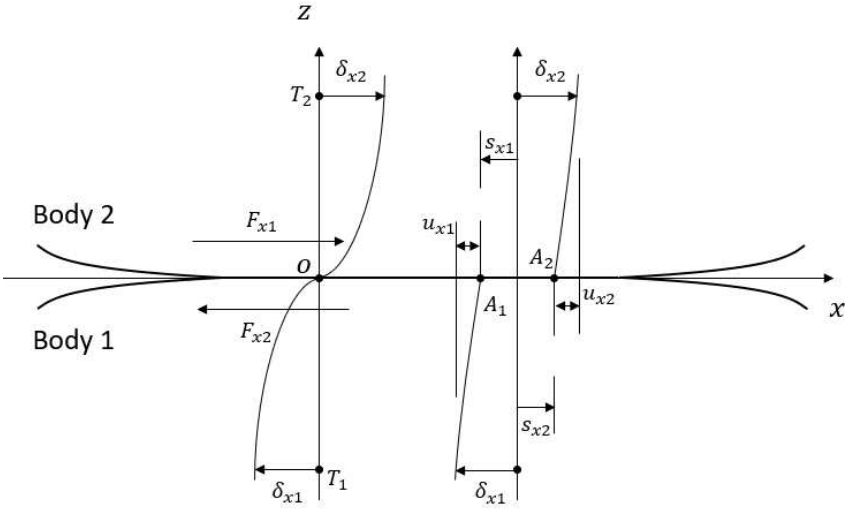

Figure 4 Displacement condition of deformation in the tangential direction: F_x is the tangential force applied to the contacting body, δ_x is the rigid body displacement in the horizontal direction, u_x is the elastic deformation in the horizontal direction of the body, s_x is the slip distance of body, and the subscripts 1 and 2 denote the contacting bodies 1 and 2 being referred respectively.

Although the Coulomb's friction law is universally applied in frictional contact modelling, there are different complementary conditions applied in the partial slip modelling which result in the presence of different algorithms as listed in Table 1. For example, some of the recent literature [19-21, 35] in Table 1 used the following criteria expressed by:

$$\begin{aligned} &|q(i,j)| \le \mu p(i,j),\ s(i,j) = 0,\ \ (i,j) \in I_s; \\ &|q(i,j)| = \mu p(i,j),\ |s(i,j)| > 0,\ q(i,j) \cdot s(i,j) < 0,\ \ (i,j) \in I_c - I_s; \end{aligned} \qquad \textbf{Equation 16}$$

In such case, the shear stress of the node in stick could be equal to the local critical value '$\mu p(i,j)$' when the node exhibits a vanishing slip distance according to the Equation 16. In this paper, we have used Equation 15 as the complementary conditions. The reason why the

equal sign is discarded in the current developed model is related to the design of the relevant algorithm for the tangential contact problem:

- For the node presenting the shear stress of '$\mu p(i,j)$', it could be either in stick or slip following the Equation 16, which depends on the corresponding nodal slip distance;
- However, the slip distance in the CGM algorithm is mathematically the residual of the linear system deriving from Equation 14, where the estimation of the rigid body indentation in tangential direction δ_x needs to be conducted in advance and it requires the identification of the stick regions;
- The complementary condition (Equation 16) leads to conflict in the algorithm since the estimation of δ_x requires the information of the system residual, where the latter is determined from the former.

This potential conflict derived from Equation 16 would be iterated in the description of the algorithm for the tangential contact model. To avoid the problem mentioned above, Chen and Wang [19] estimated δ_x with the analytical formula (Equation 30). Besides, they adjusted the rigid body translation with the difference between the computed tangential load and the prescribed load.

Author	Roughness	Method	Coulomb's friction law
Guyot et al. [13]	No	FEM+BEM	Equation 15
Chen and Wang [19]	No	SAM	Equation 16
Gallego et al. [1]	No	SAM	Equation 15
Wang et al. [20]	No	SAM	Equation 16
Spinu and Amarandei [21]	No	SAM	Equation 16
Botto et al. [27]	No	FEM	Equation 15
Dong et al. [28]	Yes	SAM	Equation 15
Bazrafshan et al. [29]	Yes	BEM	Equation 15
Alakhramsing et al. [35]	Yes	FEM+BEM	Equation 16

Table 1 List of some of work on the partial slip modelling based on Coulomb's law

2.2 Algorithm Description

One of the main difficulties in solving contact problems is that neither the contact area nor the pressure distribution is known in advance. As a result, an iterative approach or the so-called trial-and-error method is frequently applied, which starts with an assumption of a contact region and the computation of the pressure distribution and surface displacement based on the initial guess. If all the constraint conditions (Equation 10-Equation 12 for normal contact problems, Equation 13-Equation 15 for tangential contact problems) are verified by the

obtained solution, contact problems are solved. Otherwise, the contact region must be adjusted, and the new pressure distribution and surface displacement need to be computed again with the new guess. Hence, a suitable iterative scheme is essential to achieve high computational efficiency as well as accuracy. Among the potential relaxation methods, CGM was implemented in the following algorithms considering it has been widely applied to the numerical modelling of contact problems owing to its superliner rate of convergence and ensured convergence for quadratic optimization problems [17].

Apart from the iteration, the most time-consuming part during the numerical simulation of contact problems is the calculation of surface deformation (Equation 9), which always needs to be executed repeatedly in the iterative approach mentioned above. To explain it mathematically, for the contact problem discretised with a total number of N nodes, it takes N^2 multiplication operations to obtain the surface deformation in each iteration of the contact model using direct summation (DS) method. Furthermore, several iterations are often necessary for a converged solution. Therefore, the DS method becomes extremely inefficient when considering about rough surface contact as a dense grid with a fairly large number of N is required to characterize the surface roughness. According to a comparative study of numerical methods to the surface deformation calculation conducted by Wang et al. [36], DC-FFT was found to be the most efficient tool while providing a comparable numerical accuracy among the investigated methods including the DS method, DC-FFT and Multi-Level-Multi-Integration (MLMI) method, where the MLMI is another well-established technique applied in the contact solver by Keer and Polonsky [16] and the main alternative to DC-FFT advanced by Lubrecht [37]. Considering that DC-FFT can be easily implemented from the perspective of computer programming, it was applied in this model to release the computation burden when it comes to surface deformation calculation and relevant convolution processing.

The algorithms of developed models with the implementation of CGM and DC-FFT can be separated into two sections including the normal contact algorithm and the tangential contact algorithm. To simplify the description, only the tangential part is shown below as the algorithm for the normal contact is developed referring to the classical model of Polonsky and Keer [16].

The CGM algorithm for the tangential contact model is integrated with the one for normal contact model and they have a similar form shown in the flow chart in Figure 5. The highlighted sections in the flow chart are the ones that need to be modified based on the algorithm for normal elastic contact model [16]. Especially, those in blue colour are the novel parts of the developed algorithm. The detailed steps of these modified sections are described as follows:

1. The initialization of the shear stress is based on the input tangential load in x direction:

$$q(i,j) = \frac{F_x}{\Delta \cdot I_c}, \qquad \textbf{Equation 17}$$

Where I_c here denotes the number of nodes in the contacting region determined from the normal contact algorithm.

2. The tangential surface deformation is calculated from Equation 9 with DC-FFT and the estimation of the rigid body approach is calculated by:

$$\delta_x = \frac{1}{N_s} \sum_{(i,j)\in I_s} \big(u_x(i,j)\big), \qquad \textbf{Equation 18}$$

where N_s is the number of nodes in the stick region.

3. The residual of the linear system and the square Euclidean norm for the set of cells in the stick domain for the tangential contact problem is calculated as follows:

$$r_x(i,j) = u_x(i,j) - \delta_x, (i,j) \in I_c, \qquad \textbf{Equation 19}$$

$$R_x = \sum_{(i,j)\in I_s} \big(r_x(i,j)\big)^2, \qquad \textbf{Equation 20}$$

where mathematically the residual r_x is the slip distance of the node in the contact region s. The slip distance of the node in the stick region vanishes following the complementary condition. Therefore, the square Euclidean norm R_x should be approximated to zero when the algorithm converges.

It is noteworthy that the reason why the equal sign in the complementary condition is discarded is mainly related to the definition of the residual of the linear system. If the complementary condition in the literature (Equation 16) [19-21, 35] is applied here, the former estimation of the tangential rigid body approach is challenging to achieve as in the step 2 the identification of stick nodes is required where the information about slip distance of the node is necessary. However, it is also the residual of the linear system being calculated based on the estimated rigid body approach. That is why the designed algorithm is stated to be conflicting and can be hardly executed when the equal sign is included.

4. Regarding the adjustment for I_s and $I_c - I_s$ based on the complementary conditions, the following operations are conducted:

On one hand, the contact model allows no shear stress over the critical value $'\mu p'$. Consequently, the shear stress of the node in slip state exceeding the value is decreased to μp. On the other hand, if the node in the slip region exhibits a shear stress with the magnitude of μp but the product of the slip distance and the shear stress is positive, it is moved from the slip region to stick region by recalculating the nodal stress with the negative term '$-stp \cdot r_x(i,j)$'. This ensures that the stress in a stick region is always less than the critical value.

As a result, the shear stress of each cell meeting the conditions above should be adjusted as follows:

$$\text{For } I_l = \{(i,j) \in (I_c - I_s): q(i,j) > \mu p\},$$
$$q(i,j) = \mu p, \qquad (i,j) \in I_l \qquad \textbf{Equation 21}$$

$$\text{For } I_k = \{(i,j) \in (I_c - I_s): q(i,j) = \mu p, q(i,j) \cdot r_x(i,j) > 0\},$$
$$q(i,j) = q(i,j) - stp \cdot r_x(i,j), \qquad (i,j) \in I_k \qquad \textbf{Equation 22}$$

The stick domain I_s should then be modified as follows:

$$I_s = I_s \cup I_k \qquad \textbf{Equation 23}$$

When any element in the slip region is moved to stick region, a new search of the descent direction for the node must be conducted from the beginning. This operation can be achieved by the adjustment of an auxiliary variable θ in the equation of the descent direction calculation as follows:

$$d(i,j) = r_x(i,j) - d(i,j) \cdot \theta \cdot \left(\frac{R_x}{R_{old}}\right), \qquad \textbf{Equation 24}$$

where d is the search direction and R_{old} is the square Euclidean norm in the last iteration.

If I_k is empty, θ is set to one. Otherwise, it is set to zero.

5. Given that not only the shear stress of nodes in stick domain but also those in slip domain is included in the parameter q and the stress of nodes in slip region needs to remain constant (μp) without any modification, a new method is designed to enforce the static force equilibrium:

$$q(i,j) = q(i,j) + fac, (i,j) \in I_s, \qquad \textbf{Equation 25}$$

where fac is the adjusting factor determined by the following equation:

$$fac = \frac{\frac{F_x}{\Delta} - \sum_{(i,j)\in I_c} q(i,j)}{N_s}. \qquad \textbf{Equation 26}$$

A displacement-controlled algorithm is also developed for the stick-slip elastic contact model based on the one designed for the normal elastic contact model. The computational complexity of the two algorithms (load-controlled and displacement-controlled) of the tangential contact model is $O(N_1 N_2 \log(N_1 N_2))$, which is the same with the individual normal contact model as no additional factor is accounted for in this case. However, they would take more time to converge compared to the algorithm for the normal elastic contact model due to the additional integration.

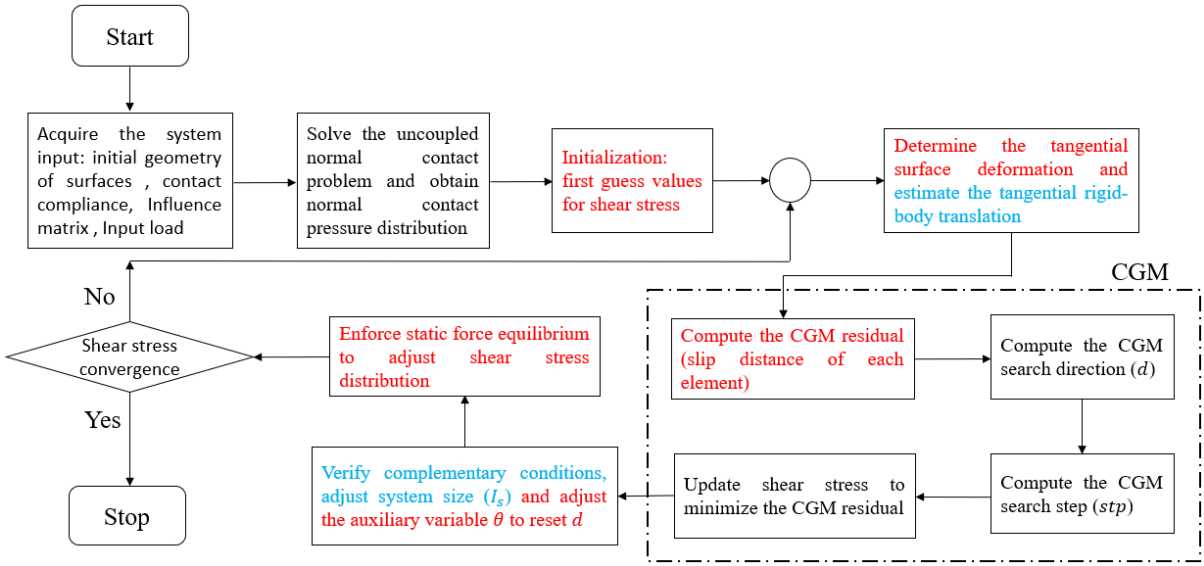

Figure 5 Flow chart of the load-controlled algorithm for the stick-slip elastic contact model

3. Model Validations and Results

The developed model was validated by comparing the simulation results with the analytical solutions. After the validation, the fully deterministic model developed here was used to study the influence of surface roughness parameters on the stick-slip separation.

3.1 Results and Validation of the Stick-Slip Contact Model

The contact of two elastic bodies made of carbon steel and discretised by 512×512 elements with the relevant parameters shown in Table 2 under the normal load of 100 N and the tangential load of 20 N was simulated.

Parameter	Value	Description
R	3500	Radius of the sphere (μm)
E_1,E_2	213	Elastic modulus of two bodies (GPa)
μ_f	0.5	Coefficient of friction
v_1,v_2	0.29	Poisson's ratio of two bodies
W_x	20	Input tangential load
W	100	Input normal load

Table 2 Parameters used in the numerical simulation

The shear stress distribution is shown in Figure 6 (a) with the stick and slip regions labelled. A three-dimensional (3D) plot of the shear stress distribution is also presented in Figure 6 (b). It

can be found that the contacting region is separated into a central region and a surrounding slip annulus in the case of the simplified single-asperity contact.

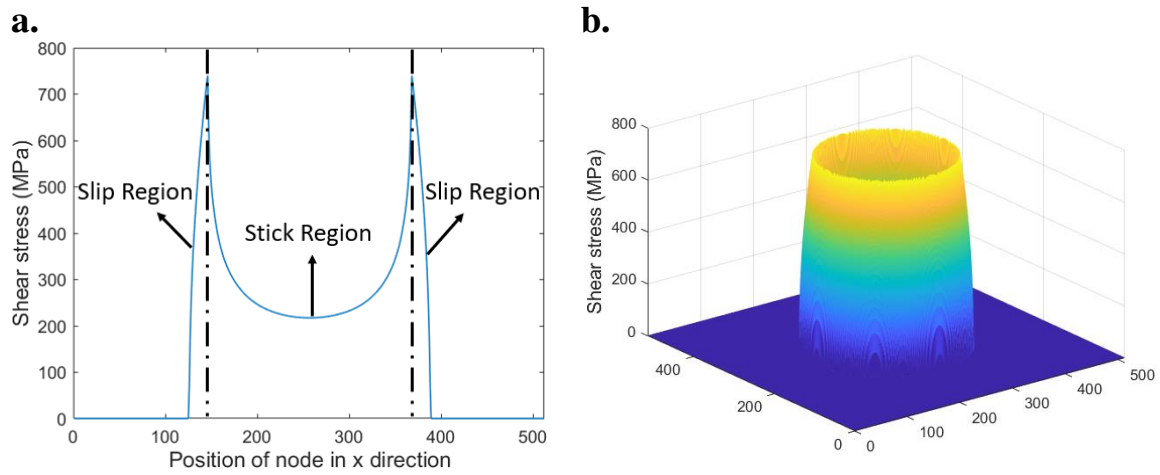

Figure 6 Simulation result under the specified input: (a) 2-D distribution of shear stress, (b) 3-D distribution of shear stress

The evolution of the circular stick region to slip region among the contacting area under the increasing tangential load was modelled as well. The non-linear response of the ratio of the stick region to the contacting region with respect to the monotonically increasing load is shown in Figure 7. The following analytical solution exhibiting a good agreement with the numerical one shown in Figure 7 was reported by Johnson [11] based on Cattaneo's theory [9]:

$$\frac{c}{a_0} = \left(1 - \frac{F_x}{\mu_f W}\right)^{\frac{1}{3}} \qquad \textbf{Equation 27}$$

$$\frac{A_{stick}}{A_{contact}} = \frac{\pi c^2}{\pi a_0^2} = \left(1 - \frac{F_x}{\mu_f W}\right)^{\frac{2}{3}} \qquad \textbf{Equation 28}$$

where A_{stick} denotes the stick area, $A_{contact}$ denotes the contacting area, c denotes the stick radius and a_0 denotes the contact radius that can be determined from the equation [11] as follows:

$$a_0 = \left(\frac{3WR}{4E^*}\right)^{\frac{1}{3}}, \qquad \textbf{Equation 29}$$

where E^* is the composite elastic modulus of the two contacting surfaces.

As observed from Figure 8 (a)-(e), the central stick region keeps shrinking with the rising tangential load while the slip annulus responds oppositely.

The computed tangential rigid body translation from the developed model was compared with the one derived from the analytical formulas [11] as follows:

$$\delta_x = \delta_0 \left[1 - \left(1 - \frac{F_x}{\mu_f W}\right)^{2/3}\right],$$

$$\delta_0 = 3\mu_f W \frac{\left[\frac{(2-v_1)(1+v_1)}{E_1} + \frac{(2-v_2)(1+v_2)}{E_2}\right]}{8a_0}, \quad \textbf{Equation 30}$$

where δ_0 is the tangential rigid body translation when the contacting is at gross sliding ($F_x = \mu_f W$).

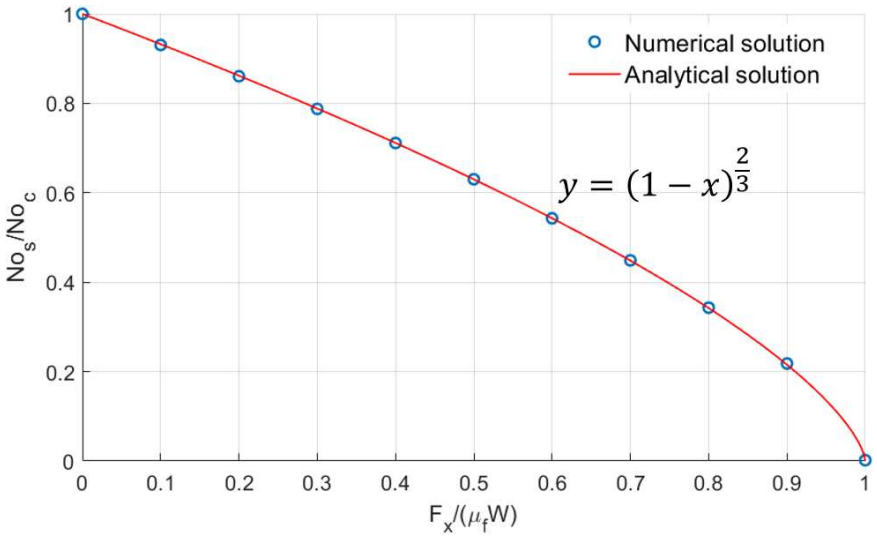

Figure 7 Evolution of ratio of the stick region to the contacting area

The comparison of the increasing tangential rigid body translation under varying tangential loads deriving from the current model and the analytical formula is shown in Figure 8 (f), where a good agreement is found.

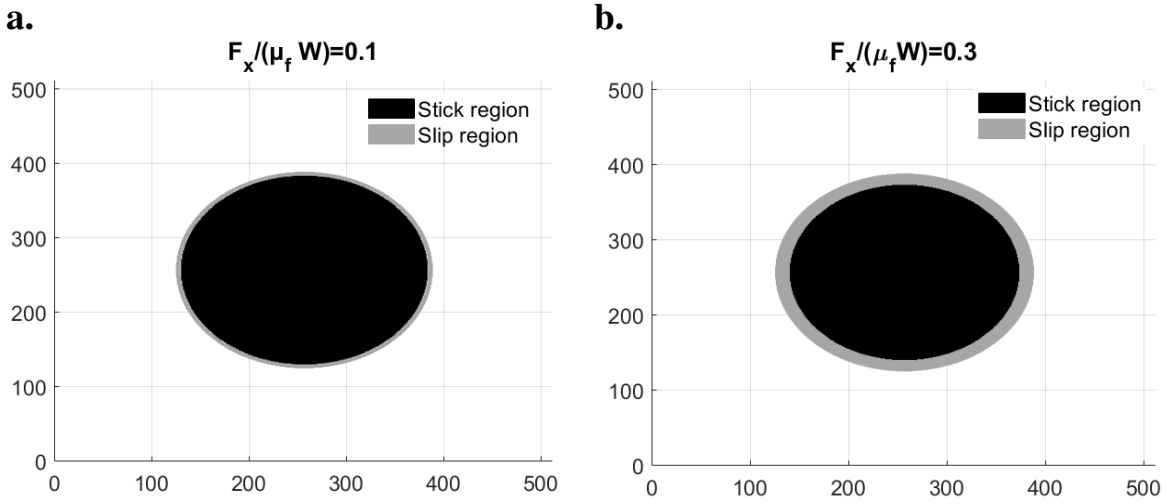

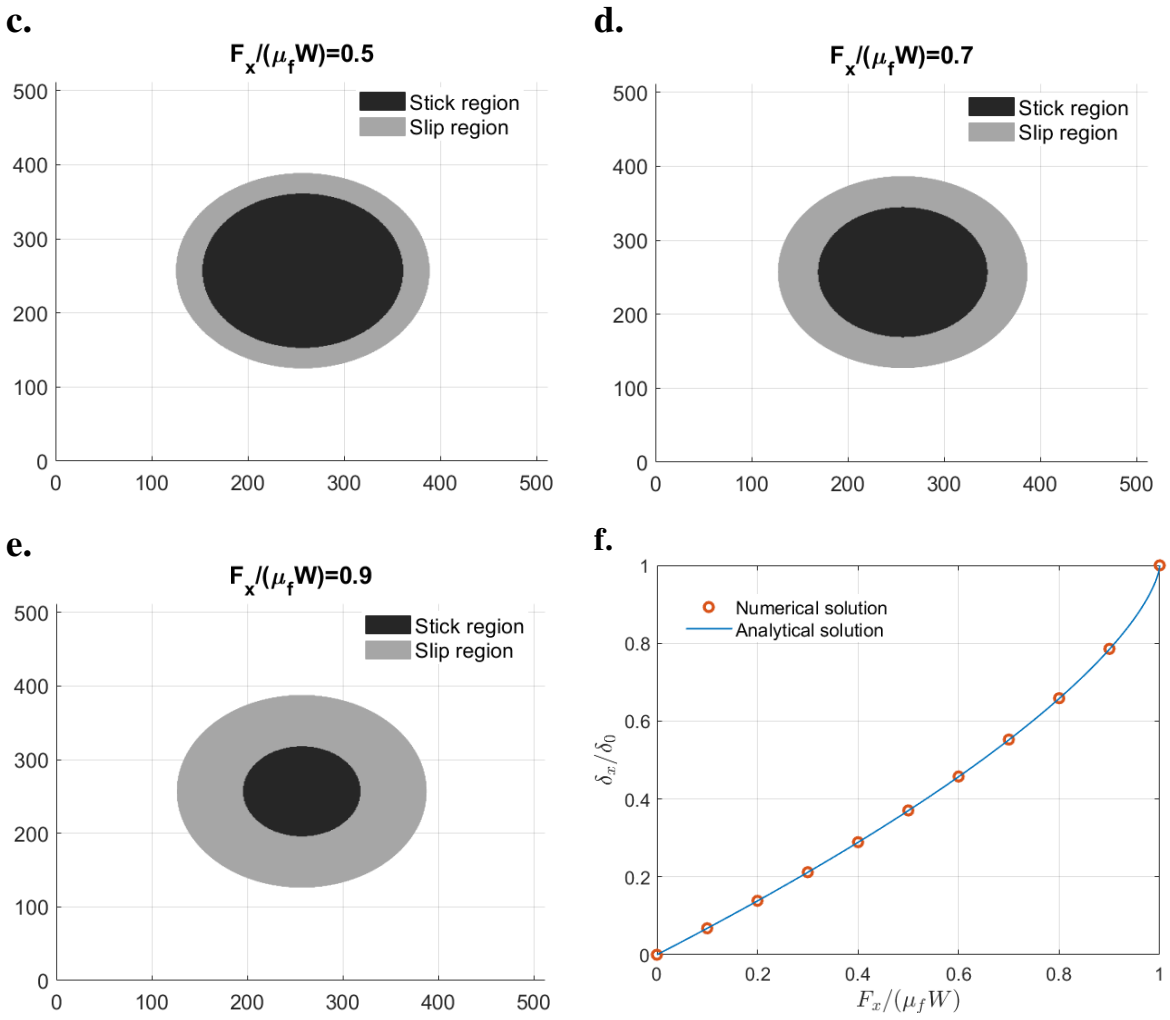

Figure 8 Results with increasing tangential loads: (a)-(e) simulated separation of stick and slip regions with increasing tangential load, (f) comparison of the growing tangential rigid body displacement with increasing tangential load deriving the developed model and the analytical method

To further validate the stick-slip model, the comparison in terms of shear stress distribution q_x was conducted as well. The analytical formula is shown as follows [11]:

$$q_x = \mu_f p_0 \left[\sqrt{1 - \left(\frac{x}{a_0}\right)^2} - H(c-x) \cdot \frac{c}{a_0} \sqrt{1 - \left(\frac{x}{c}\right)^2} \right], \qquad \textbf{Equation 31}$$

Additionally, to compare the results of the shear traction derived from the current model with the one derived from the simplified stick-slip elastic model developed by Chen and Wang [19], the μ_f was changed to 0.2 and the result is presented in Figure 9. The analytical and the numerical solutions shown in Figure 9 exhibit a great match and the similarity between Figure 9 and the plot by Chen and Wang (Fig. 4a) in [19] indicates a good agreement between the two models.

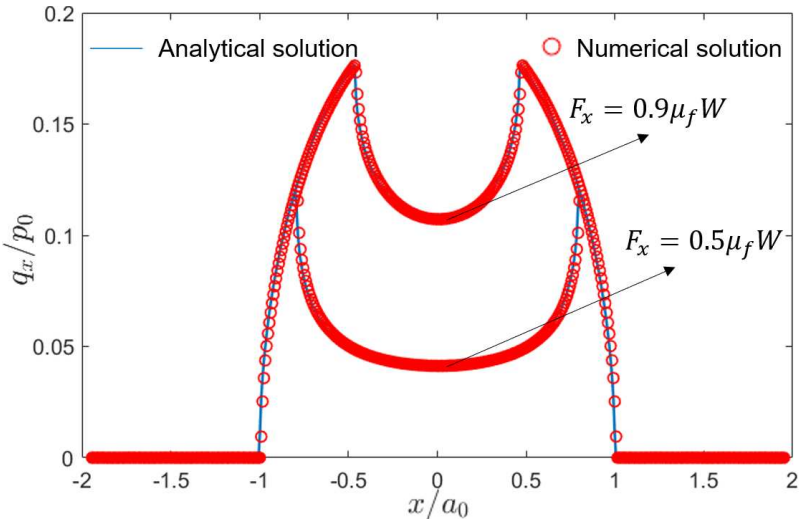

Figure 9 Comparison in terms of shear stress distribution between the numerical and analytical solutions

3.2 Simulation Results of Multi-asperity Contacts

Estimation of the real area of contact plays a central role in the tribological study in terms of adhesion, friction, lubrication and wear. Although simulation results of the contact between surfaces with simple geometries presented above are validated against the relevant analytical solutions, surfaces are always rough and irregular in practical applications. Their stochastic nature determines the area and geometry of the contacting region and subsequently affects the stiffness, electrical and thermal conductivity of the interface, friction and wear. Therefore, this surface study was extended from the single-asperity contact to multi-asperity contact, which approximates realistic rough surfaces.

3.2.1 Normal Contact of Rough Spheres

The contact between an elastic rough sphere and a smooth plane was first considered. Pastewka and Robbins [38] proposed an analytical solution that relates the variation of the real contact area to the normal load for this type of contact problem. Their parameter-free equations were later investigated by Muser [39] and were reported to have good accuracy in terms of the prediction of the real contact area (with less than 10% error). An adjusted formula was then developed for the relative contact area A_r by Muser [39] via abandoning the mean-field approximation and is given as follows:

$$A_r = \frac{A_{re}}{A_H} = \left(1 - \frac{1}{2k^2\tilde{p}^2}\right)\mathrm{erf}(k\tilde{p}) + \frac{\exp\left(-k^2\tilde{p}^2\right)}{\sqrt{\pi}k\tilde{p}}, \qquad \textbf{Equation 32}$$

where A_{re} denotes the real contact area, A_H denotes the Hertzian contact area (πa_0^2), k denotes a constant which turns out close to two for typical engineering surfaces and $\tilde{p}$ denotes the physical representation of the average contact pressure and is determined by the following equation:

$$\tilde{p} = \frac{3W}{4\sqrt{\pi}E^{*}\bar{g}a_0^2}, \qquad \textbf{Equation 33}$$

where $\bar{g}$ is the root mean square gradient of the rough surface that is often denoted as Sdq. Assume $\frac{dz(x)}{dx}$ is the slope at a specified location on the surface, then the root mean square slope of a rough surface is given by:

$$\bar{g} = \sqrt{\frac{1}{L}\int_0^L \left(\frac{d}{dx}z(x)\right)^2 dx}\,, \qquad \textbf{Equation 34}$$

where L is the sampling length.

To numerically generate the surface of the rough sphere, the smooth sphere and the micro rough surface are superimposed as shown in Figure 10. It is noted that many surfaces of interest in practice often have a self-affine fractal feature, for which each asperity has a smaller asperity on top of it at all scales. Therefore, the statistical properties of the self-affine fractal surfaces remain with a scale transformation [40, 41].

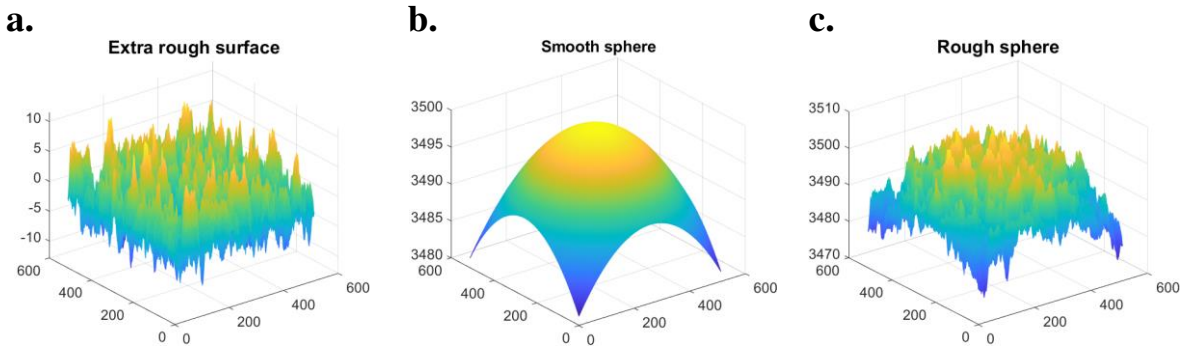

Figure 10 Generation of a rough sphere: (a) micro rough surface, (b) smooth sphere and (c) the final produced rough sphere by the combination of (a) and (b)

The micro rough surfaces with the self-affine properties in this study are generated through the power spectral density (PSD), which has the following power-law relation [42]:

$$C(q) \sim q^{-2(1+H)} \qquad \textbf{Equation 35}$$

where H here is the Hurst exponent related to the fractal dimension D_f ($H = 3 - D_f$).

Since the surface cannot be self-affine over all length scale in reality, the above relation only holds in a limited wavevector region ($q_0 < q < q_1$) resulting in a form shown in Figure 11, where q_0 and q_1 are the short-distance roll-off wavevector and the long-distance cut-off wavevector respectively and depend on the relevant system. The fractal dimension is determined by the slope of the $\log C - \log q$ plot for the section where $q > q_0$. Besides, the smallest possible wavevector q_L depends on the lateral size L of the surface under consideration ($q_L = 2\pi/L$) [40, 42].

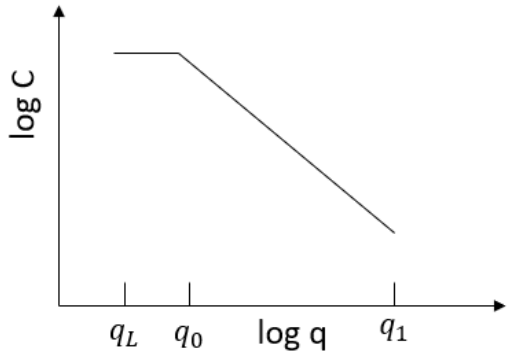

Figure 11 The PSD of a rough surface which is self-affine for $\mathbf{q_0 < q < q_1}$

By using random numbers for the Fourier transform of the height profiles ($\tilde{h}(q)$), the height spectrum (the second moment of $\tilde{h}(q)$ on average) can be defined as [42, 43]:

$$C(q) \equiv \langle|\tilde{h}(q)|^2\rangle = C(q_0) \times \begin{cases} 1 & q_L < q \leq q_0 \\ (q/q_0)^{-2(1+H)} & q_0 < q \leq q_1 \\ 0 & \text{else} \end{cases} \qquad \textbf{Equation 36}$$

The operator $\langle ... \rangle$ in Equation 36 denotes the average over different random-surface realization. It should be noted that all the surfaces generated following this method have a mean of zero in terms of the height profile ($\tilde{h}(q)$).

By defining related parameters including the root mean square roughness R_q, the Hurst exponent H, the length of topography in x direction L (assuming the length of topography in y direction is the same with that in x direction), number of nodes in x and y direction and the roll-off wavevector q_0, the artificial randomly rough surfaces could be generated.

As Equation 32 and Equation 33 suggest, the variation of the contact area with the normal load is affected by the RMS gradient of rough surfaces. Therefore, three extra rough surfaces with the same $\bar{g}$ (0.7518) but different R_q values were generated as shown in Figure 12 to validate this relation. The relevant input contact parameters are given in Table 3.

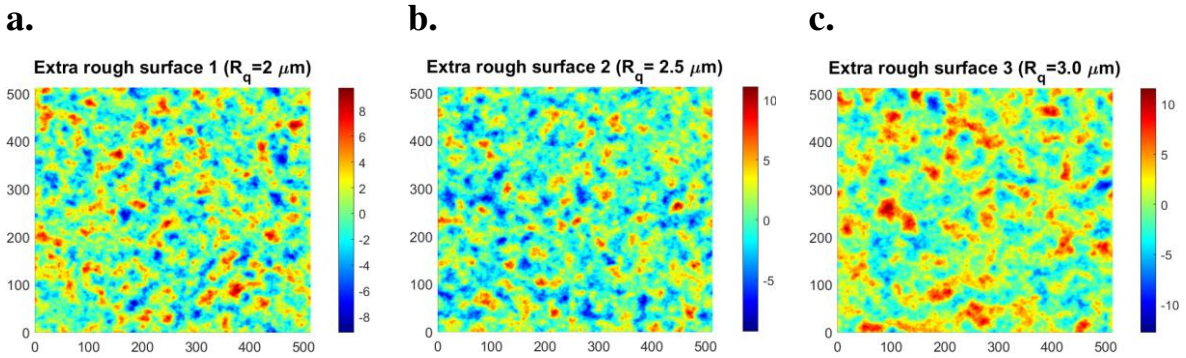

Figure 12 Generated micro rough surface with the same $\bar{g}$ but different R_q values

Parameter	Value	Description

R	3500	Radius of the smooth sphere (μm)
E_1	18.75	Elastic modulus of the sphere (MPa)
v_1	0.5	Poisson's ratio of the rough sphere
W	0.00015-0.15	Range of applied normal load (N)
L	512	Length of the surface in x and y direction (μm)

Table 3 Input parameters in the contact between the rough sphere and the smooth plane

The relation between the relative contact area A_r and the reduced contact pressure P was frequently reported by many tribologists [44, 45], where A_r is determined from the ratio of the real contact area to the Hertzian contact area and P is determined from the following equation:

$$P = \frac{W/A_H}{E^* \bar{g}}, \qquad \textbf{Equation 37}$$

where the term 'W/A_H' is known as the macroscopic pressure.

In order to show the influence of the micro-roughness added to the smooth sphere, the comparison between the Hertzian contact region and the real contact region for the rough sphere (with extra rough surface 1) under the increasing reduced pressure P is presented in Figure 13. It can be observed that there exists contacting spots outside the perimeter of the Hertzian contacting area. The reason for it is that usually only the tip of the smooth sphere comes into contact while the added roughness allows other zones out of the Hertzian area to interact with the opposite plane.

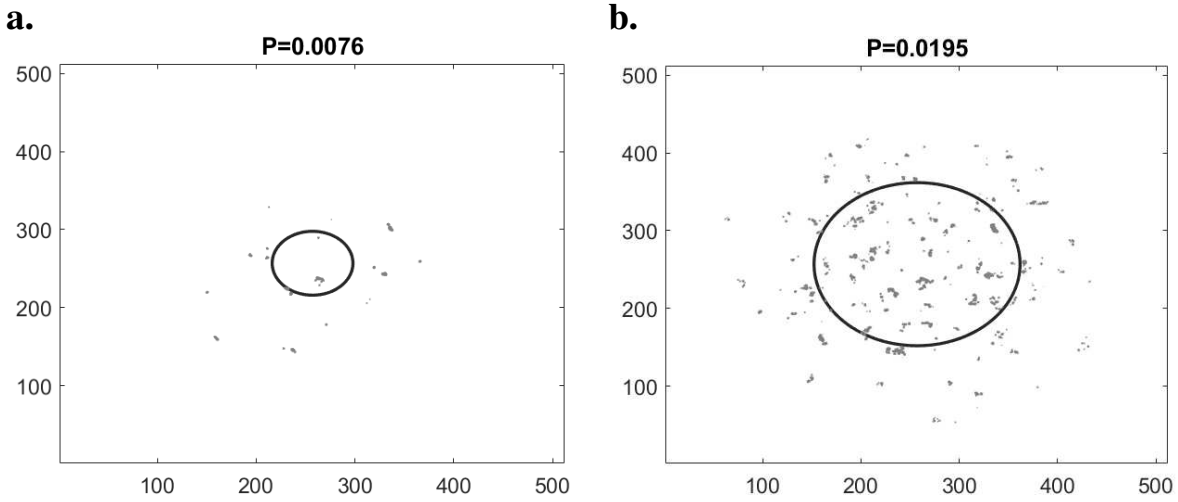

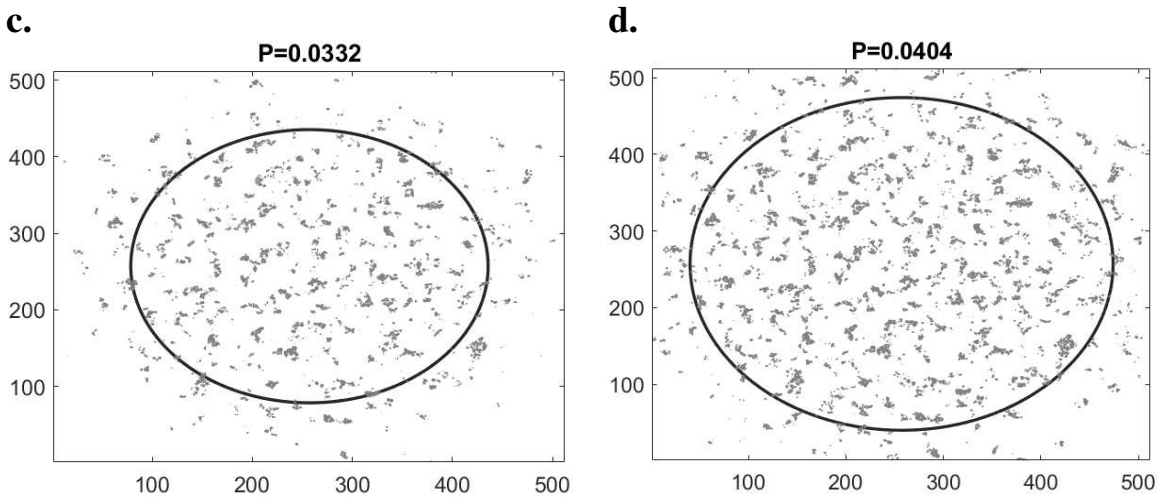

Figure 13 Comparison between the Hertzian contact area (area bounded by the solid black line) and the real contact area (grey dots) for the contact of the rough sphere (integration of the smooth sphere and the extra rough surface 1) against a smooth plane under increasing reduced pressure

The variation of the relative contact area A_r with the reduced pressure P is shown in Figure 14 for those three different rough surfaces with identical RMS gradient. The numerical solutions of the three rough sphere contacts were compared against Muser's solution derived from Equation 32 and Equation 33 [39] and a good agreement can be found. This shows that our numerical prediction is close to the solution proposed by Muser for the real contact area in rough surface contact and suggests that RMS roughness has minimal effect in this case.

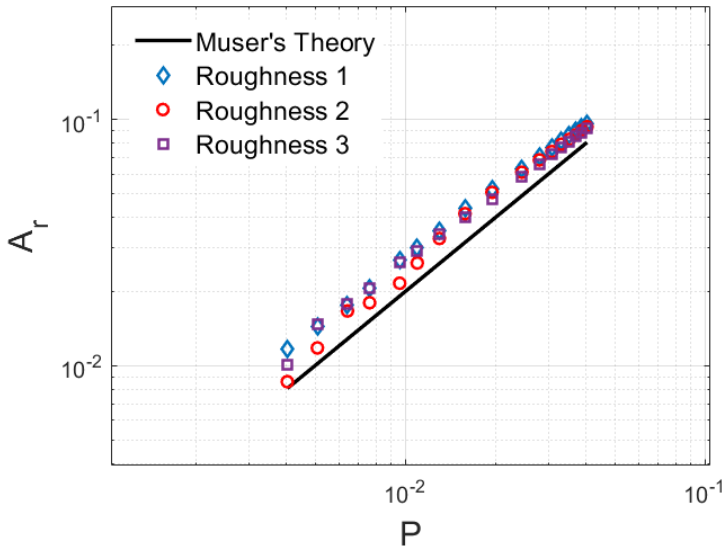

Figure 14 log-log plot of the variation of A_r with P

3.2.2 Influence of Roughness Parameters

The surface topography affects the real area of contact, which consists of both the stick and slip regions in the partial slip contact problem. To investigate the effects of the surface roughness on the separation of the stick and slip regions, the roughness parameters need to be

investigated systematically. Since the RMS roughness is one of the commonly quoted measures of surface roughness and there are numerous studies and theories reflecting on the effect of the RMS roughness on the area of contact [46, 47], adhesion [32, 48], friction [29, 49, 50] and wear [51], it was first taken into account in this paper. Besides, the role of the RMS gradient $\bar{g}$ was analysed considering its importance in determining the real contact area according to the previous studies and the analytical solutions proposed by Pastewka and Robbins [38] and Muser [39]. To increase the range of investigated surface roughness parameters, the skewness R_{sk} and kurtosis R_{ku} of rough surfaces were considered as well, where the former provides a measure of surface asymmetry and can be determined from Equation 38 while the latter offers a measure of sharpness of profile peak and can be calculated from Equation 39.

$$R_{sk} = \frac{1}{R_q^3}\frac{1}{L}\int_0^L z(x)^3 dx \qquad \textbf{Equation 38}$$

$$R_{ku} = \frac{1}{R_q^4}\frac{1}{L}\int_0^L z(x)^4 dx \qquad \textbf{Equation 39}$$

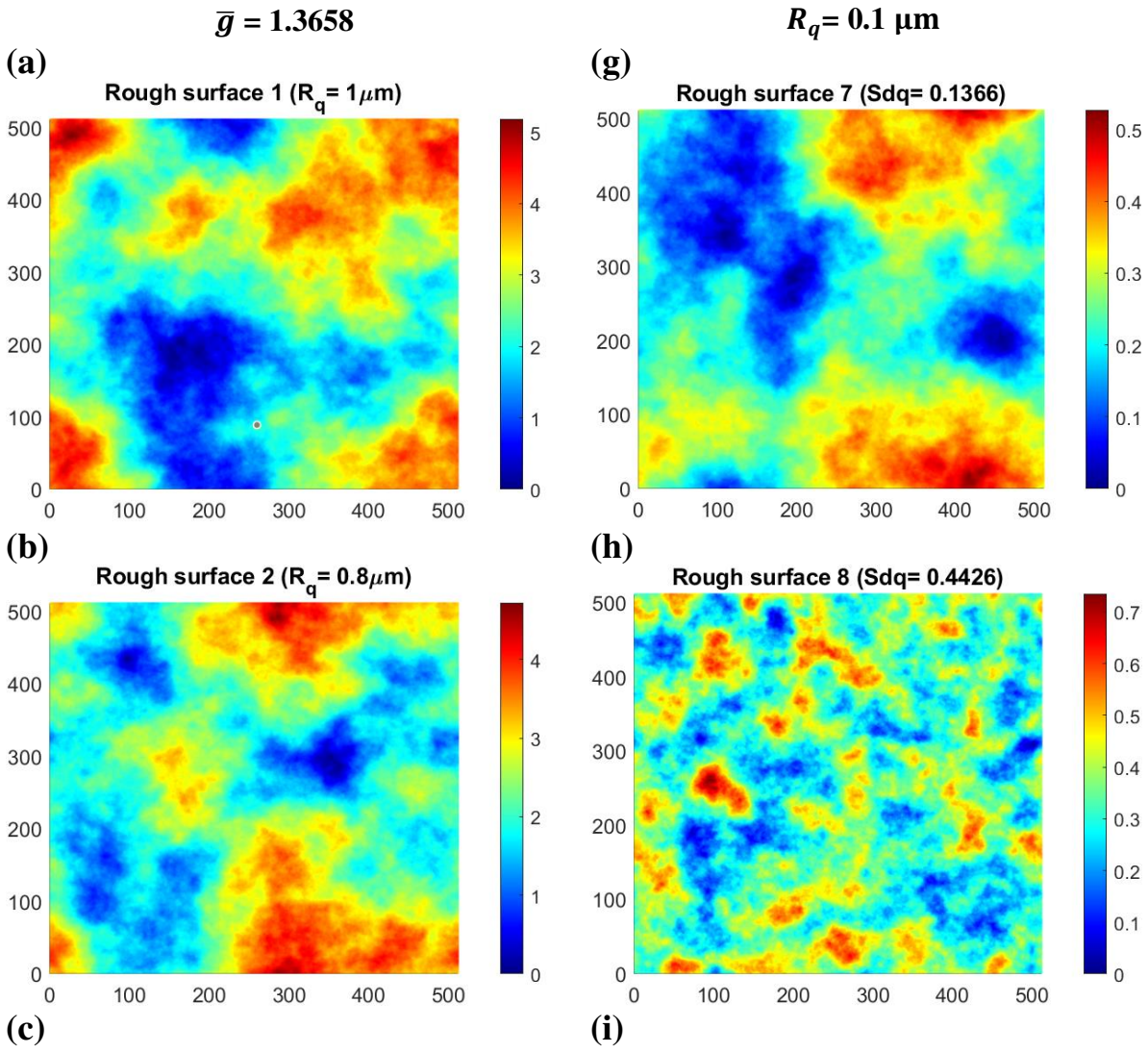

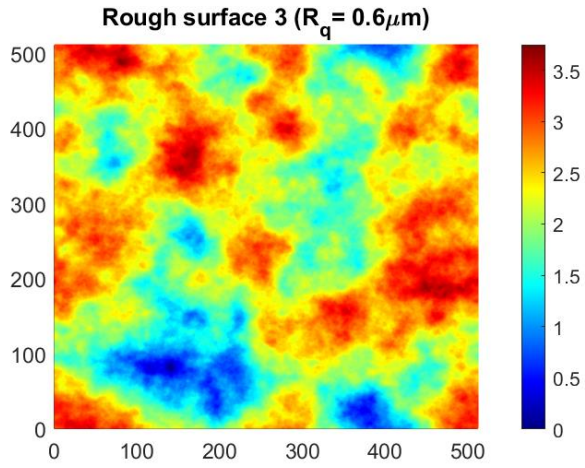
Rough surface 3 (R_q= 0.6μm)
0
100
200
300
400
500
0
0.5
1
1.5
2
2.5
3
3.5

(d)

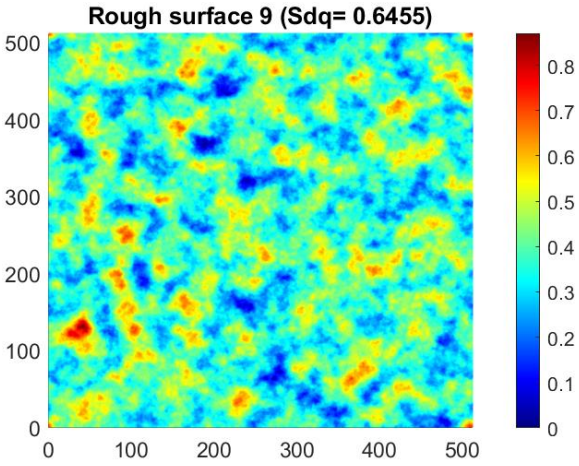
Rough surface 9 (Sdq= 0.6455)
0
100
200
300
400
500
0
0.1
0.2
0.3
0.4
0.5
0.6
0.7
0.8

(j)

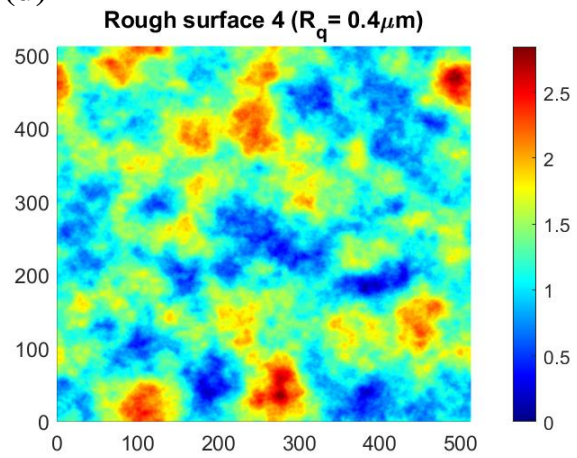
Rough surface 4 (R_q= 0.4μm)
0
100
200
300
400
500
0
0.5
1
1.5
2
2.5

(e)

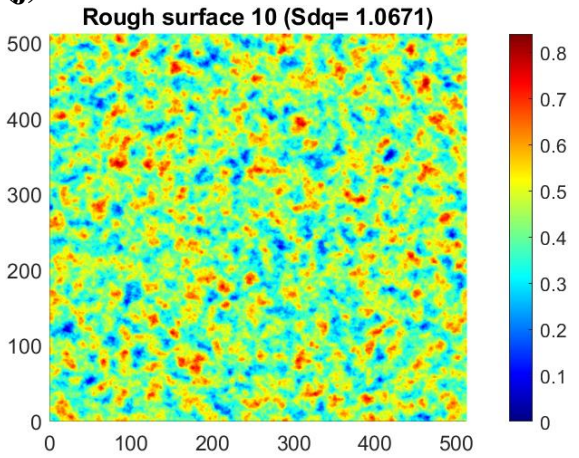
Rough surface 10 (Sdq= 1.0671)
0
100
200
300
400
500
0
0.1
0.2
0.3
0.4
0.5
0.6
0.7
0.8

(k)

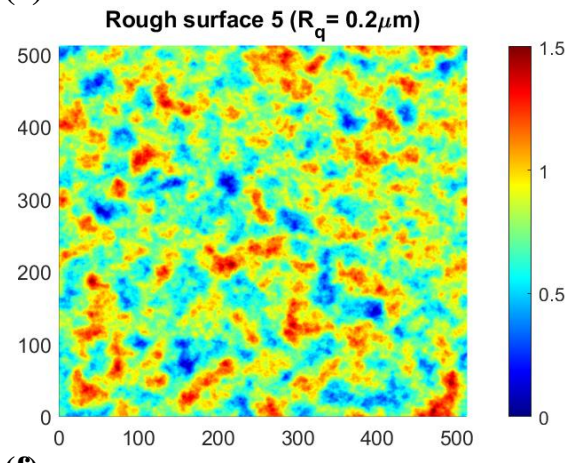
Rough surface 5 (R_q= 0.2μm)
0
100
200
300
400
500
0
0.5
1
1.5

(f)

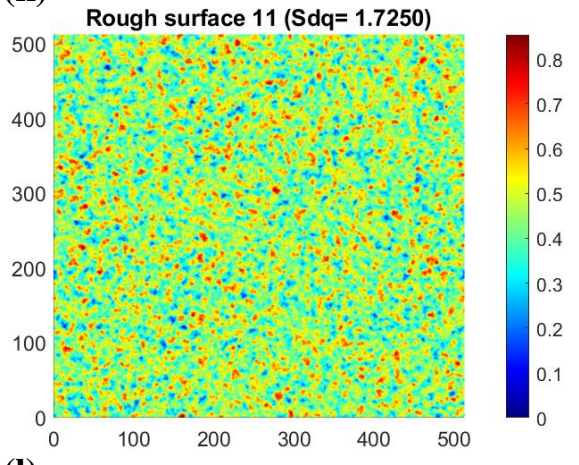
Rough surface 11 (Sdq= 1.7250)
0
100
200
300
400
500
0
0.1
0.2
0.3
0.4
0.5
0.6
0.7
0.8

(l)

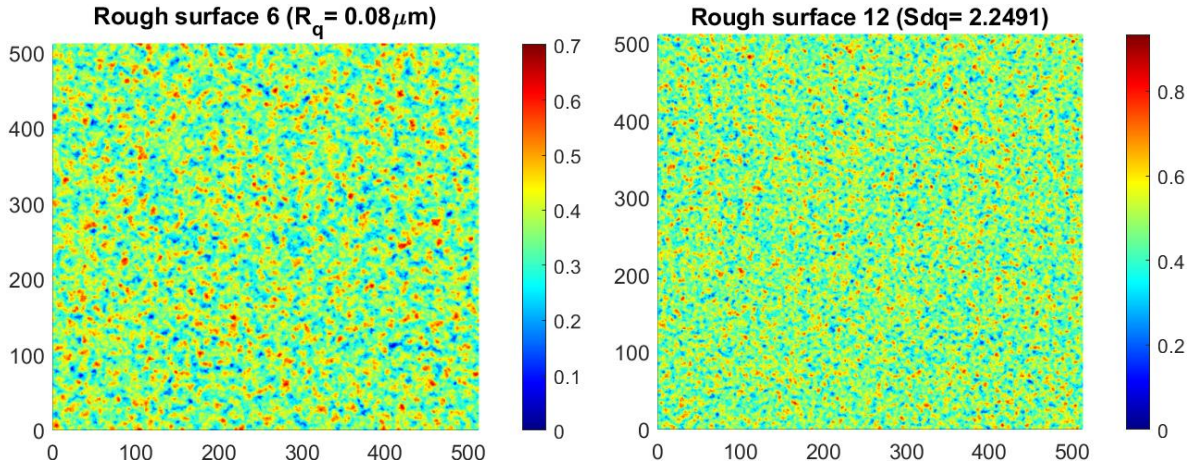

Figure 15 Generated nominally flat rough surface: (a)-(f) rough surfaces with different R_q value but the same $\bar{g}$ (1.3658) and (g)-(l) rough surfaces with different $\bar{g}$ values but the same R_q (0.1 μm)

Starting with the study of effects of RMS roughness, six nominally flat rough surfaces with different R_q values but same $\bar{g}$ as shown in Figure 15 (a)-(f) were generated. The relevant material properties and input load are shown in Table 4. The ratios of the stick and contact regions to the whole simulation domain for these contact problems under the specified inputs are shown in Figure 16 (a), where the nodes in stick or contact state are found to fluctuate around a corresponding certain value with increasing RMS roughness. Likewise, the ratio of the nodes in stick to the nodes in contact under the input RMS roughness fluctuates around 0.5 according to Figure 16 (b). Compared with that in the former case of smooth sphere contact (dash line), the proportion of the contacting region in stick decreases slightly within the range of R_q as shown in Figure 16 (b).

Parameter	Value	Description
L	100	Length of surface in x and y direction (μm)
E	18.75	Elastic modulus of the rough surface (MPa)
v	0.5	Poisson's ratio
μ_f	0.2	Coefficient of friction
W	0.0003	Applied normal load (N)
F_x	$0.5\mu_f W$	Applied tangential load (N)

Table 4 Specified material properties and input load

a. **b.**

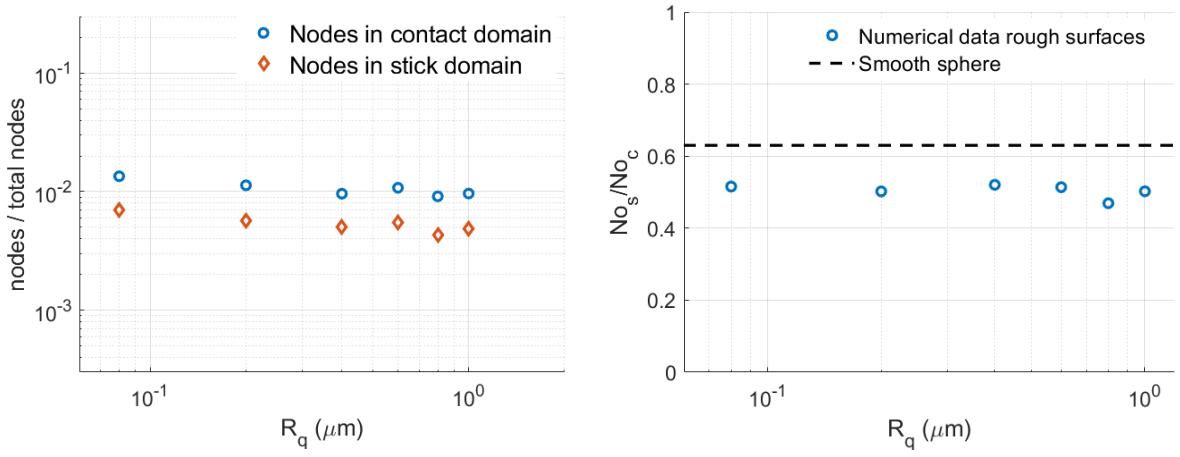

Figure 16 Simulation results under the specified R_q: (a) ratios of nodes in contact and stick regions to the whole simulation domain and (b) ratio of nodes in stick to nodes in contact

To investigate the influence of RMS gradient, six rough surfaces with different $\bar{g}$ values but the same R_q were generated as shown in Figure 15 (g)-(l). The same material properties and input load given in Table 4 were used for these rough contact problems. The ratios of the stick and contact regions to the whole simulation domain were both found to decrease significantly with increasing RMS gradient as shown in Figure 17 (a). The relationship between the logarithm of RMS gradient and the logarithm of the two ratios under the constant load is found to be quadratic as indicated in Figure 17 (a), where the trend lines using quadratic fit perfectly match the plotted data according to the theory of least-square regression ($R^2 = 1$). Notably, the decline of the contacting region with higher RMS gradient under the certain load agrees with that conclusion of the study conducted by McGhee et al. with similar surface roughness features [52]. Concerning the ratio of the nodes in stick to the nodes in contact, it fluctuates around 0.5 as shown in Figure 17 (b) and the proportion is lower than the one in the smooth sphere contact (dash line), which has similar trend as predicted by the former test with varying RMS roughness.

The skewness (R_{sk}) and kurtosis (R_{ku}) of the generated surfaces shown in Figure 15 were calculated to study their effects on the separation of stick and slip regions in the contact area. As shown in Figure 18 (a) and Figure 19 (a), the relationship between the ratio of the stick or contacting regions to the whole computational domain and the skewness (R_{sk}) or kurtosis (R_{ku}) seems to be not following any trend as expected. Besides, the ratio of the stick area to the contacting area tends to remain around 0.5 regardless of the change of these two parameters shown in Figure 18 (b) and Figure 19 (b).

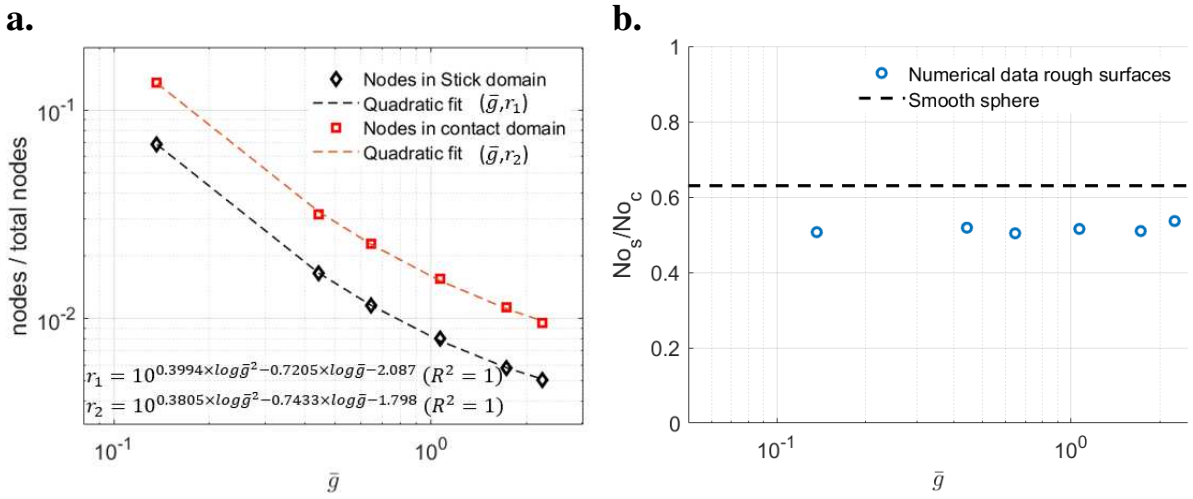

509 **Figure 17 Simulation results under the specified $\bar{g}$: (a) ratios of nodes in contact and stick**
510 **regions to the whole simulation domain and (b) ratio of nodes in stick to nodes in contact**

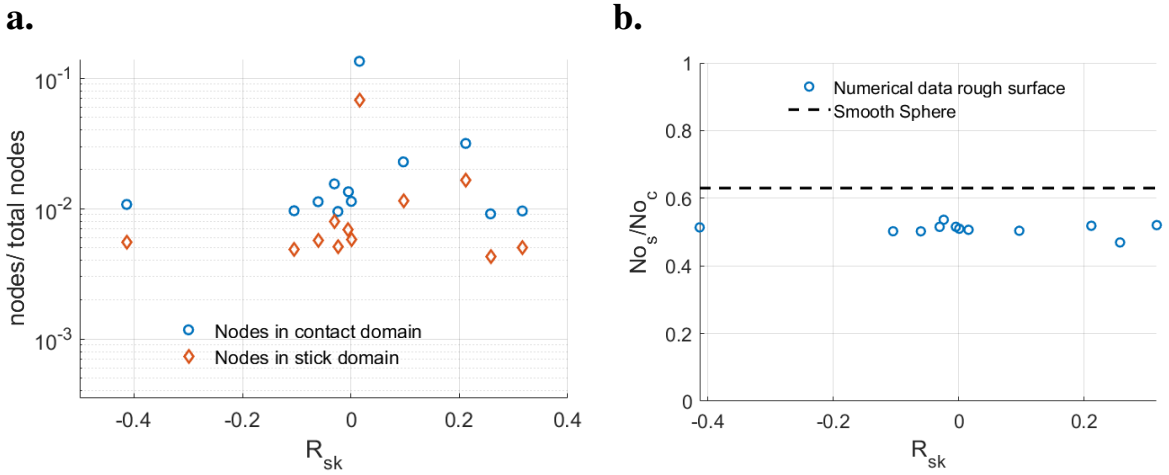

511 **Figure 18 Simulation results with varying R_{sk}: (a) ratios of nodes in contact and stick regions**
512 **to the whole simulation domain and (b) ratio of nodes in stick to nodes in contact**

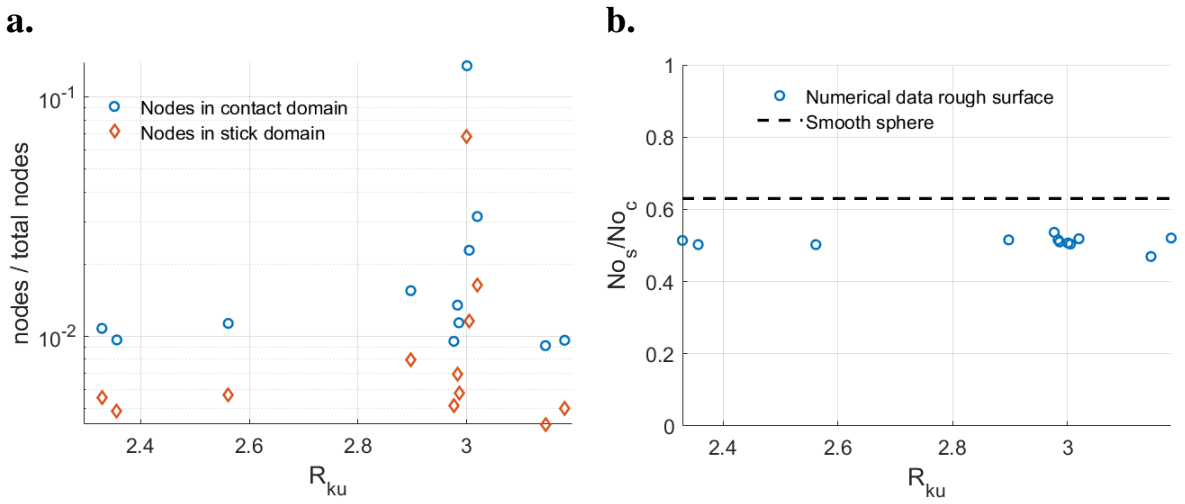

513 **Figure 19 Simulation results with varying R_{ku}: (a) ratios of nodes in contact and stick regions**
514 **to the whole simulation domain and (b) ratio of nodes in stick to nodes in contact**

515 To explain the effect of the RMS roughness on the separation of the stick and slip regions, the
516 simulation results of the rough surfaces 1 and 5 with RMS roughness of 1μm and 0.2μm
517 respectively were compared and results are presented in Figure 20 and Figure 21
518 correspondingly. It was observed clearly that the contacting patches become smaller and more
519 widely distributed with decreasing R_q from the amplified figures. This results from the fact
520 that only the highest asperities have the capacity to interact with the opposite plane for the
521 rough surface contact under small loads, which could be corresponded to the relevant rough
522 surface profile. To achieve the same RMS gradient value for the two surfaces, the short cut-off
523 wavevector of the rough surface 5 was adjusted to a high value bringing about the surface
524 profile with small-size and wide-distributed asperities. Although it leads to more contacting
525 asperities, the size of each asperity becomes smaller. As a result, the size of the total contacting
526 region remains almost constant due to the balancing of these effects. Therefore, it can be drawn
527 that what affects the contacting/stick region is the synergy of the short cut-off wavevector and
528 the RMS roughness rather than RMS roughness itself, which was also highlighted in some
529 recent theoretical work by Ciavarella et al. [48] and Violano et al. [53].

530

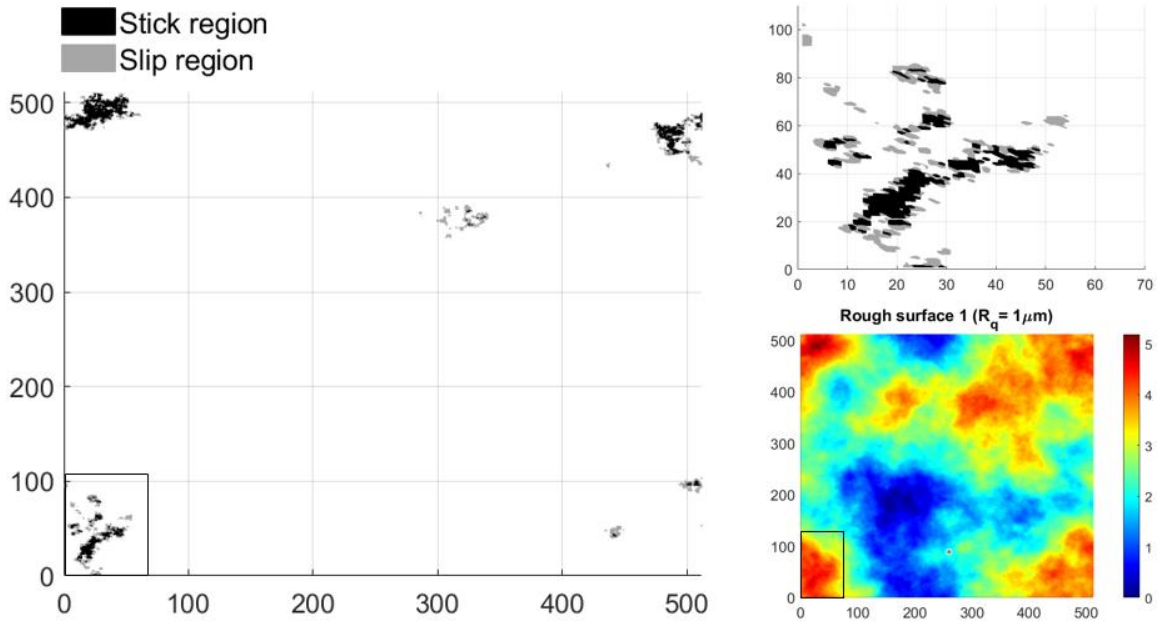

531

532 **Figure 20 Simulation results of the rough surface 1 with R_q of 1μm**

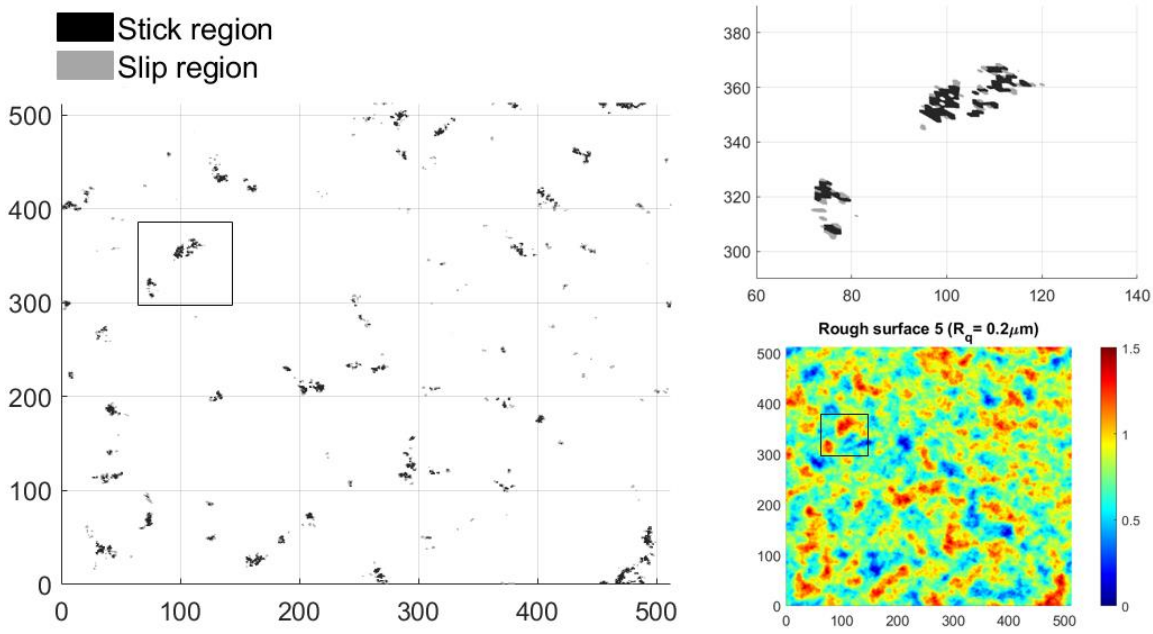

Figure 21 Simulation results of the rough surface 5 with R_q of 0.2μm

Regarding the role played by the RMS gradient, the surface asperities were found to become smaller and were distributed more intensively when the gradient increases through the comparison between the simulation results of rough surfaces 7 and 10 shown in Figure 22 and Figure 23 respectively. With the increased RMS gradient, it was found that there tend to be more individual contact spots for surface 10 as shown in Figure 23 compared to the relatively large contact islands for the surface 7 with smaller RMS gradient shown in Figure 22. However, the height of asperities in rough surface 10 was observed to become higher according to the colour bars of the two rough surface profiles, which causes a decline in the number of asperities coming into contact. Under the significant effects of the RMS gradient, there is no clear relation between the contact/stick regions and the skewness/kurtosis of the rough surface shown in Figure 18 (a) and Figure 19 (b) since the RMS gradient of these rough surfaces with increasing skewness/kurtosis changes in an irregular way.

Regardless of the response of the contacting and the stick regions to the variation of the four investigated surface roughness parameters, the ratio of the stick region to contacting region fluctuates around 0.5. Besides, the distribution of the stick and slip areas within the contact zone was found to always follow this similar pattern that for each contact spot, the slip region exists around the stick region as observed from the amplified figures shown in Figure 20-Figure 23. Inspired by the same value shared by the ratio of stick region to contact region and the ratio of the input tangential force to the friction force ($\mu_f W$), it is deduced that the input tangential load plays a dominant role in terms of the varying ratio of the stick region to contacting region for rough surface contacts irrespective of the surface roughness. To validate this opinion, the following study about the evolution of contacting region in stick with increasing tangential load was conducted.

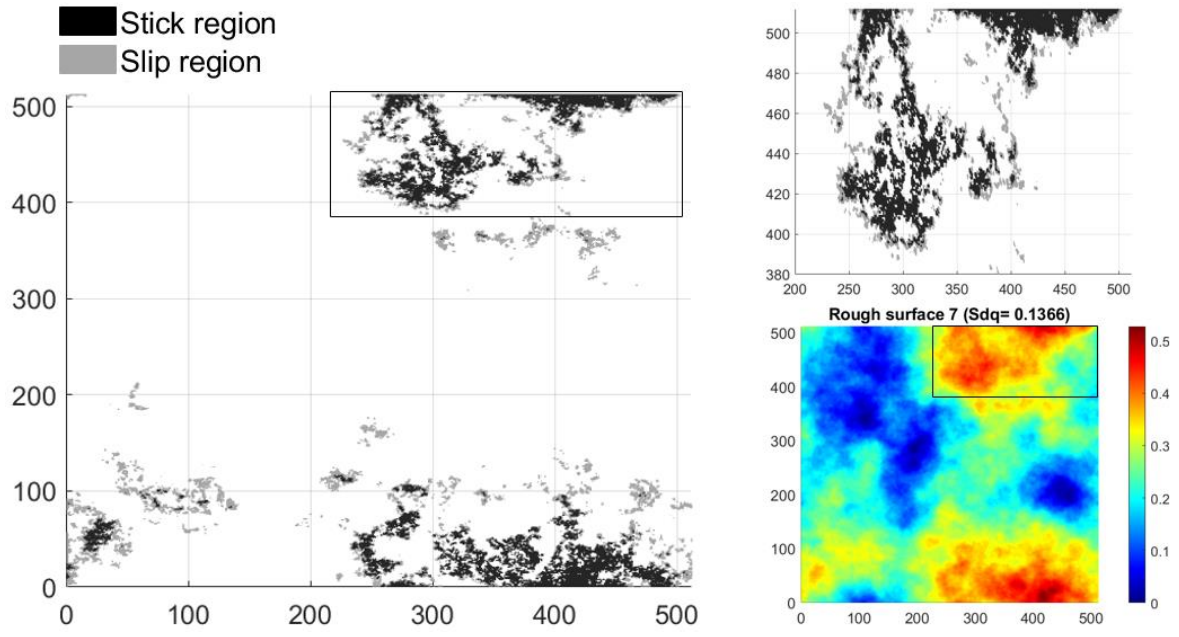

Figure 22 Simulation results of the rough surface 7 with $\bar{g}$ of 0.1366

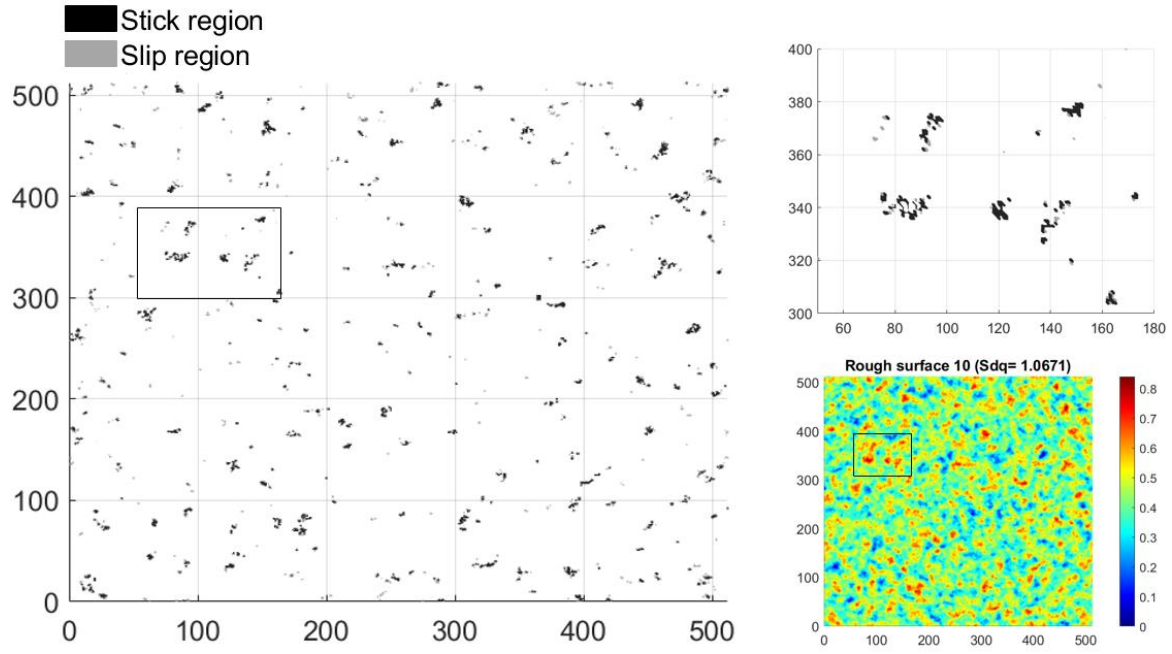

Figure 23 Simulation results of the rough surface 10 with $\bar{g}$ of 1.0671

3.2.3 Evolution of Stick Regions of Rough Surfaces

The contact between the rough surface 1 shown in Figure 15 (a) against a smooth plane under the specified material properties shown in Table 4 was first simulated while the input normal load was adjusted to $0.0025\mathrm{N}$. To study the effects of increasing tangential load on the separation of stick and slip regions for the contacting rough surfaces, the tangential load was specified to vary from 0 to $1.0\mu_f W$ with a constant interval of $0.1\mu_f W$. The separation of the stick and slip region under the tangential force of $0.2\mu_f W$ is shown in Figure 24 (b), where the

569 contact regions consisting of the stick and slip regions increase due to the higher normal load
570 compared with Figure 20. The slip regions appear at the border of the stick regions as expected
571 and are shown in the amplified Figure 24 (d) of the selected asperities, which is consistent with
572 findings in the case of the single-asperity tangential contact and multi-asperity studies discussed in
573 subsections 3.1 and 3.2.2. This common phenomenon suggests that the stick-slip contact problem
574 between a rough surface against a plane can be treated as that for numerous individual asperities
575 against a rigid plane. As a result, for each asperity in the contact state, there is a separation between
576 the stick region and slip region, where the latter is always around the periphery of the former.

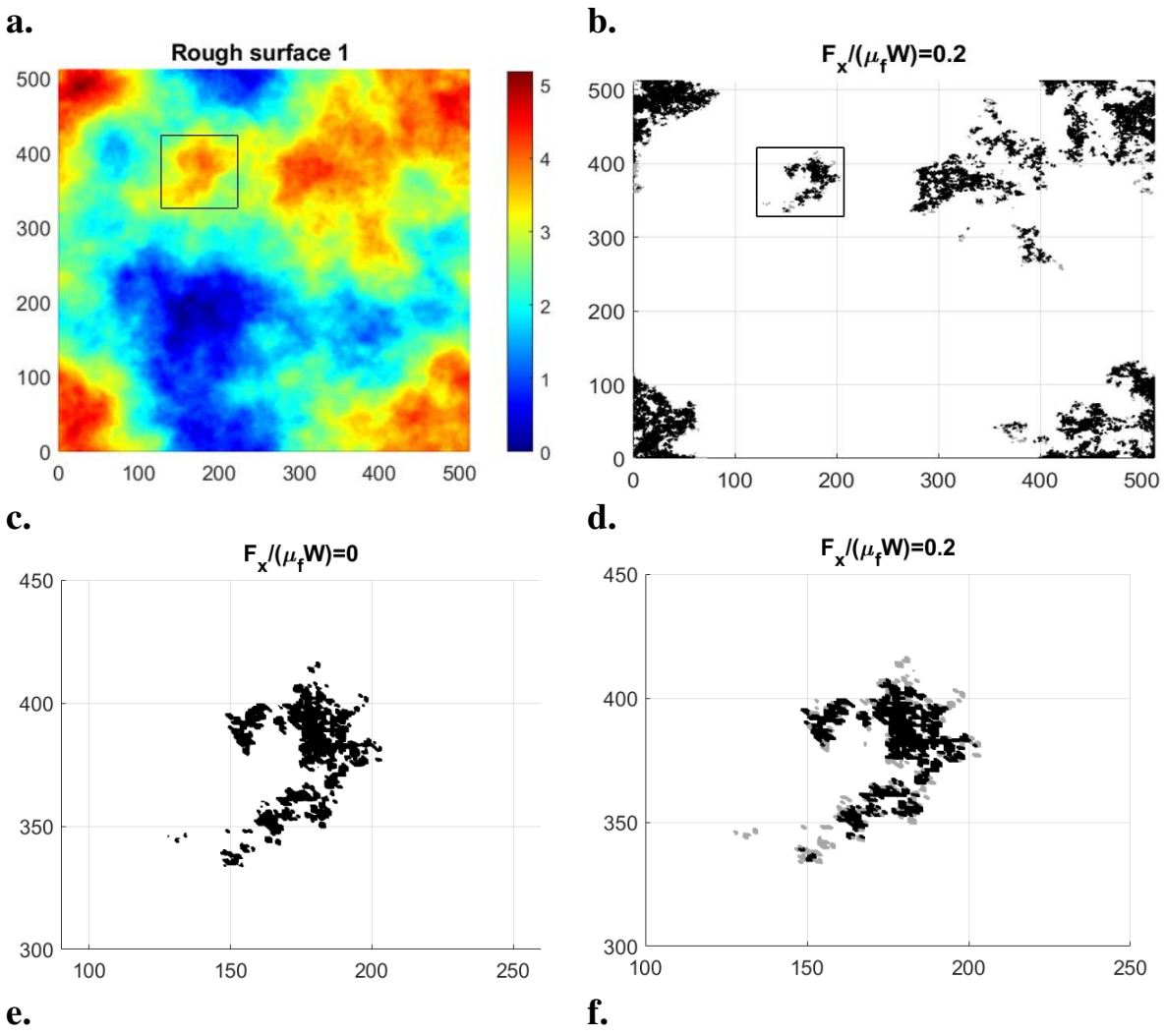

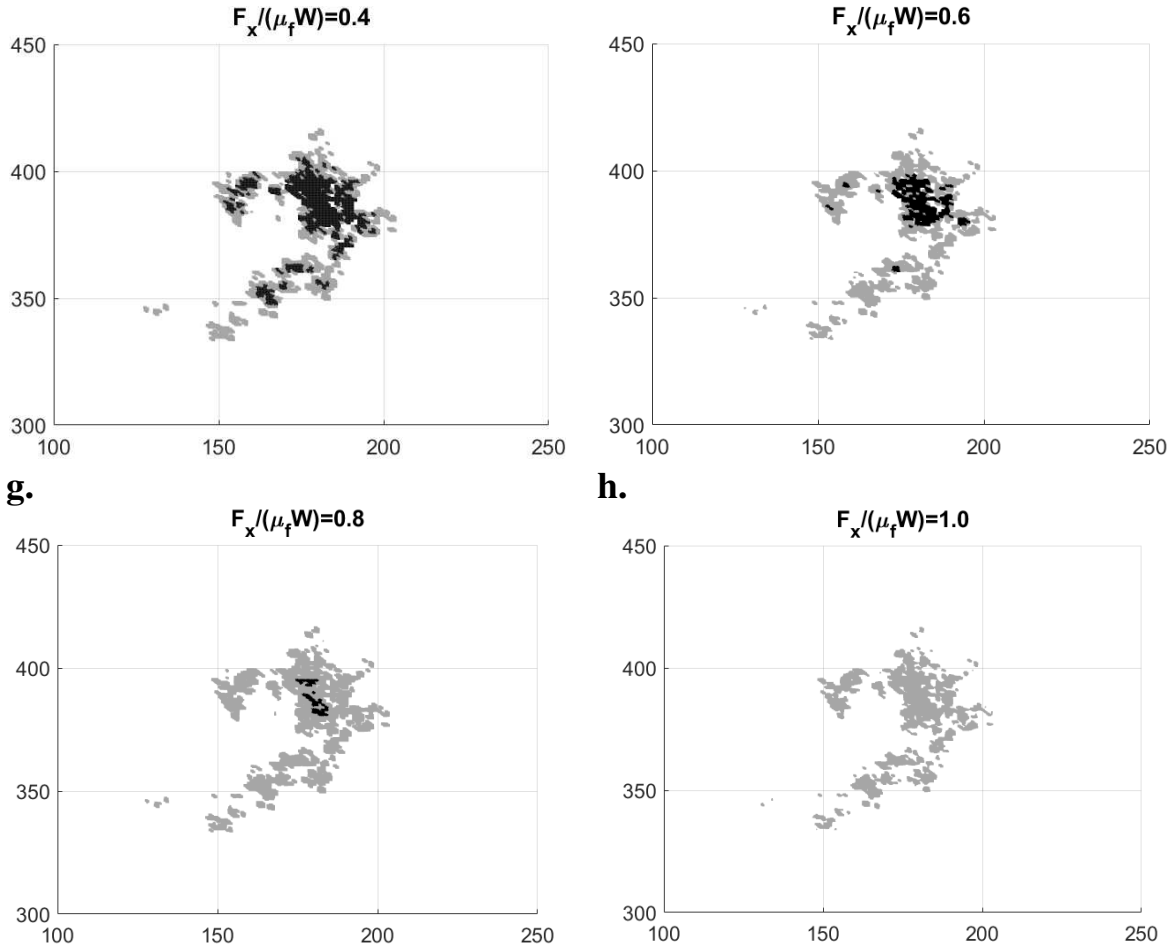

Figure 24: (a) Generate rough surface 1, (b) Simulation result under the tangential force of $0.2\mu_f W$ and (c)-(h) Separations of the stick and slip regions for the amplified sections under the increasing tangential loads

When the input tangential load increases, the separation of the stick and slip regions within the contacting area changes. The transition of the stick region to the slip region with increasing tangential load for the selected asperities was observed in those amplified figures (Figure 24 (c)-(h)). The evolution of the ratio of the nodes in stick to the nodes in contact with increasing tangential load is shown in Figure 25, where the stick region was found to decrease with increasing tangential load for this specified range. The decline was found to be linear according to the trend line using linear fitting ($\frac{\mathrm{NO_S}}{NO_c} = 1 - \frac{F_x}{\mu_f W}$). For the purpose of robustness, the rough surface 3, 7 and 9 were also investigated to check if they have the same response where the input normal loads for these studies were modified to $0.0015\mathrm{N}$, $0.0003\mathrm{N}$ and $0.0002\mathrm{N}$ respectively to obtain different contacting areas. A good agreement between the simulation results of the four conducted cases could be observed from Figure 26. Besides, the ratio of the stick region to contacting region for the rough surface contacts was found to be always lower than the one for the smooth sphere contact as the relationship between the ratio and the applied tangential load changes from non-linear (smooth) to linear (rough) as shown in Figure 26. This

explains the former finding of the decreased ratio of the stick regions to contact regions for the rough surface contact compared to the smooth sphere contact in the subsection 3.2.2.

It is noteworthy that the linearity between the ratio of the stick region to the contacting region and the tangential force for multi-asperity contacts was also found and validated by Paggi et al. [54] through their analytical analysis based on the Greenwood and Williamson model and the numerical simulation developed by Pohrt and Li [18]. Instead of the four investigated roughness parameters in the paper, the Hurst exponent of the rough surface was varied in their study. However, there was no physical interpretation presented about this transition (from non-linear to linear) for the relationship between the ratio of the stick region to contacting region and the tangential load.

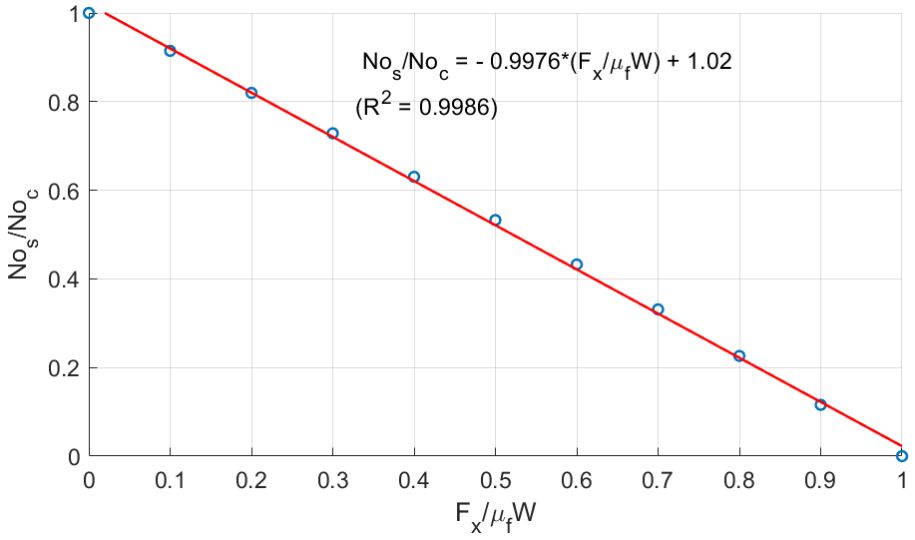

Figure 25 Evolution of the ratio of nodes in stick to nodes in contact with increasing tangential load

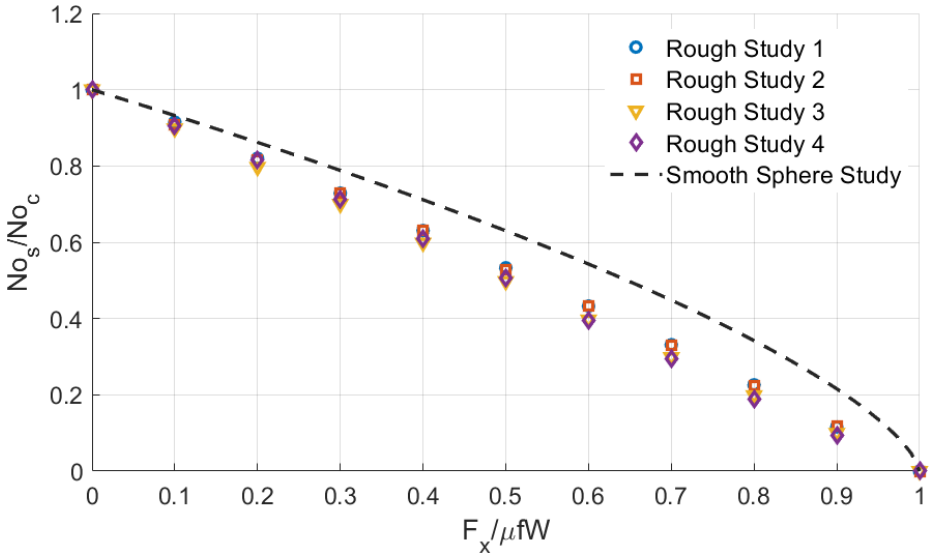

Figure 26 Evolution of the ratio of nodes in stick to nodes in contact with increasing tangential load for different rough surfaces under different normal loads

It must be noted that although the developed stick-slip model that follows the local Coulomb's friction law to determine the critical shear stress could provide valid simulation results, there exist several drawbacks of the principle. According to Chen and Wang [49], the tangential traction exceeding the shear strength of the material is unrealistic in practical problem. Besides, the constant coefficient of friction in the applied Coulomb's law fails to explain the variation trend of μ_f with the normal load and the surface roughness such as the Euler's interlocking asperity theory stating that the friction increases with the gradient of the surface asperity. As Chen and Wang suggested [49], the local shear stress deriving from the Tabor equation could be used as the alternative cut-off limit of the shear traction and this step would be taken in the future.

In addition, the validation of the developed model is all based on the well-established analytical solutions. The single-asperity contact was validated by the Hertzian-type (sphere-contact) stick-slip solutions. As to its reliability for multi-asperity contact problems, only the normal contact component of the model was validated by Muser's solution to rough sphere contact problems for lack of any analytical solutions and available experimental data for this type of partial slip contact problems. Although theoretically there should be no restrictions on the shape or configuration of contacting bodies, the validation work needs to be extended to consider different contact configuration such as cylinder contact and include several experimental work in the future to verify the capability of the model strictly.

Another future work is to further the developed stick-slip model from purely elastic contact to viscoelastic contact considering that viscoelastic materials have been extensively used in many engineering fields. When it comes to viscoelastic contact problems, the adhesive force plays a non-trivial role owing to the low contact compliance and soft feature of viscoelastic materials. Therefore, the effects of adhesion must be taken into consideration during the viscoelastic contact modelling. A viscoelastic normal contact model has been already developed by following the elastic-viscoelastic correspondence principle and validated by relevant analytical solutions. Its extension to a viscoelastic partial slip problem is the subject of current ongoing work.

4. Conclusion

In this work, a numerical model without any dependence on analytical contact formulas was developed to simulate the stick-slip contact of two elastically similar surfaces. By following the Coulomb's law described in the stick-slip theory of Ciavarella, a new algorithm to accommodate the complementary condition was developed to identify the stick and slip regions

within the contacting area. Although only results of the load-controlled algorithm are presented in the paper, it is quite convenient to achieve the displacement-controlled ones for rough surface contact problems. Owing to the application of well-estimated computational techniques including DC-FFT and CGM, this model can provide valid solutions to the stick-slip contact problems in a short time (normally 40 seconds for smooth sphere contact problems and 140 seconds for rough surface contact problems with 512×512 nodes using a desktop PC).

Regarding the study of rough surfaces based on the developed partial slip model, the following conclusions are drawn:

- The contacting region and the stick region are unaffected by the RMS roughness of rough surfaces under certain loads (normal and tangential) while the RMS gradient is kept constant. This can be achieved by altering the short cut-off wavevector and RMS roughness simultaneously;
- Unlike the role of the RMS roughness, the RMS gradient evidently affects the contact region and stick region such that a higher RMS gradient leads to the decline of the contact area and the stick regions under constant load; an equation is proposed to identify the region of stick and the region of total contact with respect to RMS slope.
- Under the significant effects of the RMS gradient, the relationship between the skewness or kurtosis and the contacting/stick region is irregular;
- The ratio of the stick area to the total contacting area depends on the applied tangential load and is insensitive to the four roughness parameters (RMS roughness, RMS slope, skewness and kurtosis). Instead of the non-linear trend in the smooth Hertzian-type partial slip contact, the relationship between the ratio of the stick to contacting regions and the tangential load becomes linear when it comes to rough surface contacts. This is an important finding since identifying the ratio of stick and slip is important in determining friction and wear in many engineering applications.

Acknowledgement

The authors are thankful to the school of mechanical engineering at the University of Leeds for supporting this study by funding the PhD studentship of Dongze Wang.

Appendix A

The influence coefficient matrix was obtained via the full solution of the Boussinesq. The discretized form of solutions was achieved through integrating over the small rectangular mesh area of $2a \times 2b$ as follows:

$$C^{zz} = \frac{1-\nu}{2\pi G}\{(x+a)In[\frac{(y+b)+\sqrt{(y+b)^2+(x+a)^2}}{(y-b)+\sqrt{(y-b)^2+(x+a)^2}}] + (y+b)In[\frac{(x+b)+\sqrt{(y+b)^2+(x+a)^2}}{(x-a)+\sqrt{(y+b)^2+(x-a)^2}}] + (x-a)In[\frac{(y-b)+\sqrt{(y-b)^2+(x-a)^2}}{y+b)+\sqrt{(y+b)^2+(x-a)^2}}] + (y-b)In[\frac{(x-a)+\sqrt{(y-b)^2+(x-a)^2}}{(x+a)+\sqrt{(y-b)^2+(x+a)^2}}]\};$$

$$C^{yy} = \frac{1}{2\pi G}\{(x+a)In[\frac{(y+b)+\sqrt{(y+b)^2+(x+a)^2}}{(y-b)+\sqrt{(y-b)^2+(x+a)^2}}] + (1-v)(y+b)In[\frac{(x+b)+\sqrt{(y+b)^2+(x+a)^2}}{(x-a)+\sqrt{(y+b)^2+(x-a)^2}}] + (x-a)In[\frac{(y-b)+\sqrt{(y-b)^2+(x-a)^2}}{y+b)+\sqrt{(y+b)^2+(x-a)^2}}] + (1-v)(y-b)In[\frac{(x-a)+\sqrt{(y-b)^2+(x-a)^2}}{(x+a)+\sqrt{(y-b)^2+(x+a)^2}}]\};$$

$$C^{xx} = \frac{1}{2\pi G}\{(1-v)(x+a)In[\frac{(y+b)+\sqrt{(y+b)^2+(x+a)^2}}{(y-b)+\sqrt{(y-b)^2+(x+a)^2}}] + (y+b)In[\frac{(x+b)+\sqrt{(y+b)^2+(x+a)^2}}{(x-a)+\sqrt{(y+b)^2+(x-a)^2}}] + (1-v)(x-a)In[\frac{(y-b)+\sqrt{(y-b)^2+(x-a)^2}}{y+b)+\sqrt{(y+b)^2+(x-a)^2}}] + (y-b)In[\frac{(x-a)+\sqrt{(y-b)^2+(x-a)^2}}{(x+a)+\sqrt{(y-b)^2+(x+a)^2}}]\};$$

$$C^{zx} = \frac{1-2v}{4\pi G}\{(y+b)In[\frac{\sqrt{(y+b)^2+(x+a)^2}}{\sqrt{(y+b)^2+(x-a)^2}}] + (y-b)In[\frac{\sqrt{(y-b)^2+(x-a)^2}}{\sqrt{(y-b)^2+(x+a)^2}}] + (x+a)[\tan^{-1}\frac{y+b}{x+a} - \tan^{-1}\frac{y-b}{x+a}] + (x-a)[\tan^{-1}\frac{y-b}{x-a} - \tan^{-1}\frac{y+b}{x-a}];$$

$$C^{xz} = -C^{zx};$$

$$C^{zy} = \frac{1-2v}{4\pi G}\{(x+a)In[\frac{\sqrt{(y+b)^2+(x+a)^2}}{\sqrt{(y-b)^2+(x+a)^2}}] + (x-a)In[\frac{\sqrt{(y-b)^2+(x-a)^2}}{\sqrt{(y+b)^2+(x-a)^2}}] + (y+b)[\tan^{-1}\frac{x+a}{y+b} - \tan^{-1}\frac{x-a}{y+b}] + (y-b)[\tan^{-1}\frac{x-a}{y-b} - \tan^{-1}\frac{x+a}{y-b}];$$

$$C^{yz} = -C^{zy};$$

$$C^{xy} = \frac{v}{2\pi G}\left[\sqrt{(y-b)^2+(x+a)^2} - \sqrt{(y-b)^2+(x-a)^2} + \sqrt{(y+b)^2+(x-a)^2} - \sqrt{(y+b)^2+(x+a)^2}\right];$$

$$C^{yx} = C^{xy}.$$

Appendix B

The material properties including the elastic modulus and Poisson's ratio given in Table 2 were used to determine the influence matrix C_{xx} and C_{yx}. The relatively large difference in the order of magnitude between these two is shown in Figure 27.

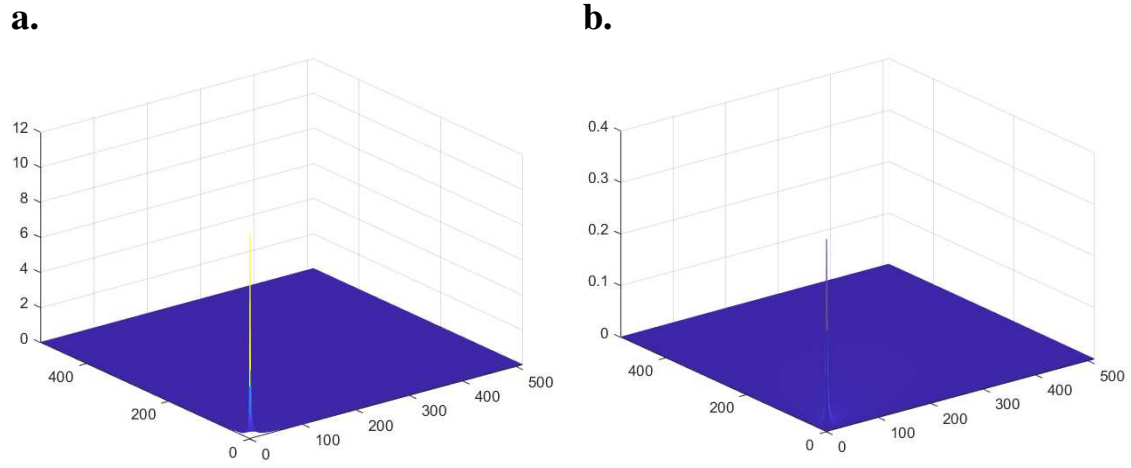

Figure 27 Comparison of the influence matrices: (a) C_{xx} and (b) C_{yx}

Reference

[1] L. Gallego, D. Nélias, S. Deyber, A fast and efficient contact algorithm for fretting problems applied to fretting modes I, II and III, Wear, 268 (2010) 208-222.
[2] L. Gallego, D. Nélias, Modeling of Fretting Wear Under Gross Slip and Partial Slip Conditions, Journal of Tribology, 129 (2007) 528-535.
[3] Y. Fukahori, P. Gabriel, J.J.C. Busfield, How does rubber truly slide between Schallamach waves and stick–slip motion?, Wear, 269 (2010) 854-866.
[4] X.C. Wang, J.L. Mo, H. Ouyang, X.D. Lu, B. Huang, Z. Zhou, The effects of grooved rubber blocks on stick–slip and wear behaviours, Proceedings of the Institution of Mechanical Engineers, Part D: Journal of Automobile Engineering, 233 (2019) 2939-2954.
[5] P. Bagga, G. Brisson, A. Baldwin, C.E. Davies, Stick-slip behavior of dairy powders: Temperature effects, Powder Technology, 223 (2012) 46-51.
[6] J. Tichy, B. Bou-Saïd, A Stick-Slip Model Based on Granular Flow Theory, Tribology Letters, 67 (2018) 14.
[7] A. Pant, G.V. Ramana, M. Datta, Stick-slip behavior of dry fly ash, Particulate Science and Technology, 38 (2020) 605-616.
[8] K. Viswanathan, N.K. Sundaram, Distinct stick-slip modes in adhesive polymer interfaces, Wear, 376-377 (2017) 1271-1278.
[9] C. Cattaneo, Sul contatto di due corpi elstici: Distribuzione locale degli sforzi, Reconditi dell Accademia natzionale dei Lincei, 27 (1938) 342-348, 474–478, 434–436.
[10] R.D. Mindlin, Compliance of elastic bodies in contact, ASME J. Appl. Mech., 16 (1949) 259-268.
[11] K.L. Johnson, Contact Mechanics, Cambridge University Press, Cambridge, 1985.
[12] F. Kosior, N. Guyot, G. Maurice, Analysis of frictional contact problem using boundary element method and domain decomposition method, International Journal for Numerical Methods in Engineering, 46 (1999) 65-82.
[13] N. Guyot, F. Kosior, G. Maurice, Coupling of finite elements and boundary elements methods for study of the frictional contact problem, Computer Methods in Applied Mechanics and Engineering, 181 (2000) 147-159.
[14] V. Brizmer, Y. Kligerman, I. Etsion, The effect of contact conditions and material properties on the elasticity terminus of a spherical contact, International Journal of Solids and Structures, 43 (2006) 5736-5749.
[15] V. Brizmer, Y. Kligerman, I. Etsion, Elastic-plastic spherical contact under combined normal and tangential loading in full stick, Tribology Letters, 25 (2007) 61-70.
[16] I.A. Polonsky, L.M. Keer, A numerical method for solving rough contact problems based on the multi-level multi-summation and conjugate gradient techniques, Wear, 231 (1999) 206-219.
[17] Q. Wang, Interfacial mechanics : theories and methods for contact and lubrication, CRC Press, Taylor & Francis Group, Boca Raton, 2020.
[18] R. Pohrt, Q. Li, Complete boundary element formulation for normal and tangential contact problems, Physical Mesomechanics, 17 (2014) 334-340.
[19] W.W. Chen, Q.J. Wang, A numerical model for the point contact of dissimilar materials considering tangential tractions, Mechanics of Materials, 40 (2008) 936-948.
[20] Z.-J. Wang, W.-Z. Wang, H. Wang, D. Zhu, Y.-Z. Hu, Partial Slip Contact Analysis on Three-Dimensional Elastic Layered Half Space, Journal of Tribology, 132 (2010).
[21] S. Spinu, D. Amarandei, Numerical Simulation of Slip-Stick Elastic Contact, in: M. Andriychuk (Ed.) Numerical Simulation - From Theory to Industry, IntechOpen2012.
[22] J. Armand, L. Salles, C.W. Schwingshackl, Numerical Simulation of Partial Slip Contact Using a Semi-Analytical Method, American Society of Mechanical Engineers, 2015.
[23] M. Ciavarella, The generalized Cattaneo partial slip plane contact problem. I—Theory, International Journal of Solids and Structures, 35 (1998) 2349-2362.

749 [24] M. Ciavarella, D.A. Hills, R. Moobola, Analysis of plane and rough contacts, subject to a
750 shearing force, International Journal of Mechanical Sciences, 41 (1999) 107-120.
751 [25] M. Ciavarella, Tangential Loading of General Three-Dimensional Contacts, Journal of
752 Applied Mechanics, 65 (1998) 998-1003.
753 [26] L. Gallego, B. Fulleringer, S. Deyber, D. Nélias, Multiscale computation of fretting wear
754 at the blade/disk interface, Tribology International, 43 (2010) 708-718.
755 [27] D. Botto, M. Lavella, A numerical method to solve the normal and tangential contact
756 problem of elastic bodies, Wear, 330-331 (2015) 629-635.
757 [28] Q. Dong, K. Zhou, W.W. Chen, Q. Fan, Partial slip contact modeling of heterogeneous
758 elasto-plastic materials, International Journal of Mechanical Sciences, 114 (2016) 98-110.
759 [29] M. Bazrafshan, M.B. de Rooij, D.J. Schipper, On the role of adhesion and roughness in
760 stick-slip transition at the contact of two bodies: A numerical study, Tribology International,
761 121 (2018) 381-388.
762 [30] X. Tian, B. Bhushan, A Numerical Three-Dimensional Model for the Contact of Rough
763 Surfaces by Variational Principle, Journal of Tribology, 118 (1996) 33-42.
764 [31] A. Ghanbarzadeh, M. Wilson, A. Morina, D. Dowson, A. Neville, Development of a new
765 mechano-chemical model in boundary lubrication, Tribology International, 93 (2016) 573-582.
766 [32] A. Ghanbarzadeh, M. Faraji, A. Neville, Deterministic normal contact of rough surfaces
767 with adhesion using a surface integral method, Proceedings of the Royal Society A:
768 Mathematical, Physical and Engineering Sciences, 476 (2020) 20200281.
769 [33] M. Ciavarella, J. Joe, A. Papangelo, J.R. Barber, The role of adhesion in contact
770 mechanics, Journal of The Royal Society Interface, 16 (2019) 20180738.
771 [34] R.M. McMeeking, M. Ciavarella, G. Cricrì, K.-S. Kim, The Interaction of Frictional Slip
772 and Adhesion for a Stiff Sphere on a Compliant Substrate, Journal of Applied Mechanics, 87
773 (2020).
774 [35] S.S. Alakhramsing, M.B. de Rooij, M. van Drogen, D.J. Schipper, The influence of stick–
775 slip transitions in mixed-friction predictions of heavily loaded cam–roller contacts,
776 Proceedings of the Institution of Mechanical Engineers, Part J: Journal of Engineering
777 Tribology, 233 (2019) 676-691.
778 [36] W.Z. Wang, H. Wang, Y.C. Liu, Y.Z. Hu, D. Zhu, A comparative study of the methods
779 for calculation of surface elastic deformation, Proceedings of the Institution of Mechanical
780 Engineers, Part J: Journal of Engineering Tribology, 217 (2003) 145-154.
781 [37] A.A. Lubrecht, A Fast Solution of the Dry Contact Problem and the Associated Subsurface
782 Stress Field, Using Multilevel Techniques, ASME J. Tribol., 113 (1991) 128-133.
783 [38] L. Pastewka, M.O. Robbins, Contact area of rough spheres: Large scale simulations and
784 simple scaling laws, Applied Physics Letters, 108 (2016) 221601.
785 [39] M.H. Müser, On the Contact Area of Nominally Flat Hertzian Contacts, Tribology Letters,
786 64 (2016) 14.
787 [40] B.N.J. Persson, Contact mechanics for randomly rough surfaces, Surface Science Reports,
788 61 (2006) 201-227.
789 [41] C. Putignano, L. Afferrante, G. Carbone, G. Demelio, A new efficient numerical method
790 for contact mechanics of rough surfaces, International Journal of Solids and Structures, 49
791 (2012) 338-343.
792 [42] B.N.J. Persson, O. Albohr, U. Tartaglino, A.I. Volokitin, E. Tosatti, On the nature of
793 surface roughness with application to contact mechanics, sealing, rubber friction and adhesion,
794 Journal of physics. Condensed matter : an Institute of Physics journal, 17 (2005) R1-R62.
795 [43] T.D.B. Jacobs, T. Junge, L. Pastewka, Quantitative characterization of surface topography
796 using spectral analysis, Surface Topography: Metrology and Properties, 5 (2017) 013001.
797 [44] M.H. Müser, W.B. Dapp, R. Bugnicourt, P. Sainsot, N. Lesaffre, T.A. Lubrecht, B.N.J.
798 Persson, K. Harris, A. Bennett, K. Schulze, S. Rohde, P. Ifju, W.G. Sawyer, T. Angelini, H.

Ashtari Esfahani, M. Kadkhodaei, S. Akbarzadeh, J.-J. Wu, G. Vorlaufer, A. Vernes, S. Solhjoo, A.I. Vakis, R.L. Jackson, Y. Xu, J. Streator, A. Rostami, D. Dini, S. Medina, G. Carbone, F. Bottiglione, L. Afferrante, J. Monti, L. Pastewka, M.O. Robbins, J.A. Greenwood, Meeting the Contact-Mechanics Challenge, Tribology Letters, 65 (2017) 118.

[45] V.A. Yastrebov, G. Anciaux, J.-F. Molinari, From infinitesimal to full contact between rough surfaces: Evolution of the contact area, International Journal of Solids and Structures, 52 (2015) 83-102.

[46] M.P. Rapetto, A. Almqvist, R. Larsson, P.M. Lugt, On the influence of surface roughness on real area of contact in normal, dry, friction free, rough contact by using a neural network, Wear, 266 (2009) 592-595.

[47] B.B. Zugelj, M. Kalin, Submicron-scale experimental analyses of multi-asperity contacts with different roughnesses, Tribology International, 119 (2018) 667-671.

[48] M. Ciavarella, Universal features in “stickiness” criteria for soft adhesion with rough surfaces, Tribology International, 146 (2020) 106031.

[49] W.W. Chen, Q.J. Wang, A Numerical Static Friction Model for Spherical Contacts of Rough Surfaces, Influence of Load, Material, and Roughness, Journal of Tribology, 131 (2009).

[50] M. Bazrafshan, M. Rooij, D.J. Schipper, The Effect of Adhesion and Roughness on Friction Hysteresis Loops, International Journal of Mechanical Sciences, 155 (2019).

[51] A. Ghosh, F. Sadeghi, A novel approach to model effects of surface roughness parameters on wear, Wear, 338-339 (2015) 73-94.

[52] A.J. McGhee, A.A. Pitenis, A.I. Bennett, K.L. Harris, K.D. Schulze, J.M. Urueña, P.G. Ifju, T.E. Angelini, M.H. Müser, W.G. Sawyer, Contact and Deformation of Randomly Rough Surfaces with Varying Root-Mean-Square Gradient, Tribology Letters, 65 (2017) 157.

[53] G. Violano, L. Afferrante, A. Papangelo, M. Ciavarella, On stickiness of multiscale randomly rough surfaces, The Journal of Adhesion, DOI 10.1080/00218464.2019.1685384(2019) 1-19.

[54] M. Paggi, R. Pohrt, V.L. Popov, Partial-slip frictional response of rough surfaces, Scientific Reports, 4 (2014) 5178.